Proceedings of the Project Review, Geo-Mathematical Imaging Group (Purdue University, West Lafayette IN),
Vol. 1 (2012) pp. 97-121.

# MASSIVELY PARALLEL STRUCTURED MULTIFRONTAL SOLVER FOR TIME-HARMONIC ELASTIC WAVES IN 3D ANISOTROPIC MEDIA

SHEN WANG*, MAARTEN V. DE HOOP†, JIANLIN XIA‡, AND XIAOYE S. LI§

**Abstract.** We present a massively parallel structured multifrontal solver for the equations describing time-harmonic elastic waves in 3D anisotropic media. We use a multi-component second-order finite-difference method. We extend the corresponding stencil to enhance the accuracy of the discretization without increasing the order. This accuracy is aligned with the tolerance level used for the Hierarchically SemiSeparable (HSS) low rank matrix compression underlying our solver. The interplay between the finite accuracy discretization and the finite accuracy matrix solver yields the key strategy which leads to the architecture of our algorithm. We analyze the relevant matrix structures, (numerically) estimate the rank of the dense matrices prior to the HSS compression and study the effect of anisotropy, and deduce the complexity and storage requirements of our algorithm.

**Key words.** time-harmonic elastic waves – structured multifrontal solver

**1. Introduction.** We consider the modeling of time-harmonic elastic waves in anisotropic media. We use a multi-component finite-difference method. In this paper, we are concerned with solving the resulting algebraic equations for a large number of different right-hand sides, that is, surface or subsurface sources, on a large domain in the context of modeling seismic wave propagation with applications in reverse time migration (RTM) based inverse scattering [5] and local optimization based full waveform inversion (FWI) in mind. The key result is the development of a massively parallel structured direct solver accommodating anisotropy in the low to mid-frequency range.

In smoothly varying media, we can diagonalize the system of equations describing elastic waves using pseudodifferential operators – assuming it is of principal type – thus decoupling the polarizations (for example, see [16]). We can then consider time-harmonic solutions of scalar equations. This involves the application of techniques from microlocal analysis. In general, the polarized wave equations are scalar pseudodifferential equations of second order, the discretizations of which require particular techniques; wavelet bases provide a way to carry this out in principle [3]. Here, we are not concerned with such discretization techniques and instead solve the original coupled system of equations, with limited smoothness conditions. More importantly, we do *not* impose the restriction to systems of *real principal type*. However, if the system were of principal type, we can use the mentioned diagonalizing operators to decouple the polarizations in the solution of the system. We will show an example of the effectiveness of such a procedure.

We use a second-order finite difference scheme for the discretization of the system of equations, together with an optimization technique which involves adding more points to the basic stencil, to minimize the numerical dispersion. In principle, such an optimization procedure can be carried out at each spatial point following the heterogeneity and changing anisotropy in the medium. Our dispersion analysis and numerical examples demonstrate that with only five grid points per shear wavelength, we can achieve at least 4 digits of accuracy. This accuracy is aligned with the tolerance level used for the Hierarchically SemiSeparable (HSS) low rank matrix compression underlying our solver. The interplay between the finite accuracy discretization and the finite accuracy matrix solver yields the key strategy which leads to the architecture of our algorithm.

The direct method of choice for solving the mentioned problem is the multifrontal factorization algorithm [13]. The central idea of the multifrontal algorithm is to reorganize the sparse factorization of the discretized matrix operator into a series of dense local factorizations; this algorithm is also used in MUMPS [1]. The algorithm is used together with the method of nested dissection [10] to obtain a nested hierarchical structure and generate a $LU$ factorization from the bottom up to minimize fill-ins. In nested dissection, separators are introduced to recursively divide the mesh into two disjoint subdomains. Each separator consists of a small set of mesh points. The nested partitioning leads to a sequence of separators at different levels, which forms a binary tree. This tree is used in the multifrontal method to manage the factorization from the bottom up, level by level.

*Department of Mathematics, Purdue University, West Lafayette, IN 47907.
†Center for Computational and Applied Mathemematics, Purdue University, West Lafayette, IN 47907 (mdehoop@purdue.edu).
‡Department of Mathematics, Purdue University, West Lafayette, IN 47907.
§Computational Research Division, Lawrence Berkeley National Laboratory (LBNL).

The development, here, for *systems* of equations is a generalization of the work of [21, 22, 24] concerning *scalar* equations including nested dissection with separators of variable thickness. We follow the approach developed by [27, 28] of integrating the multifrontal method with structured matrices. The fill-in blocks of the factorization appear to be highly compressible using the framework of HSS matrices. Compression is a critical component to reduce memory requirements and enables the solution of problems defined on large subsurface domains; the accuracy of the solution is controlled and can be limited in the applications considered. We analyze the relevant matrix structures, (numerically) estimate the rank of the dense matrices prior to the HSS compression and study the effect of anisotropy, and deduce the complexity and storage requirements of our algorithm; we then compare these with the Helmholtz equation for polarized waves in isotropic media.

The solver developed, here, opens up the way to speed up significantly adjoint state computations in seismic applications for the purpose of full waveform inversion with a large number of events [18]. A strategy for time-harmonic full waveform inversion making use of a multifrontal solver for scalar waves was developed by [14]. Another application of our solver concerns the numerical implementation of the novel notion of array receiver functions introduced by [5]. Our current algorithm has been developed on a Cartesian grid, but the modifications to spherical sections is straightforward [18, 8].

We compare the accuracy of our algorithm with time-domain Discontinous Galerkin (DG) method. We mention related and alternative developments. For isotropic media, [15] developed a finite-difference method for modeling time-harmonic elastic waves. [9] designed a non-conforming finite-element discretization emphasizing viscoelastic rheology, (see also [12]). In fact, our solver can be adapted to a finite element method straightforwardly. [2] developed an *iterative* solver based on an algebraic multigrid method and FEM in the isotropic case with a damping preconditioner. For a time-domain counterpart, we mention the work of [4]. For the high-frequency scattering of elastic waves, we refer to the work of [7] based on PUFEM involving wavelet based $ILU$ preconditioners.

The outline of the paper is as follows. In the next section, we summarize the relevant equations, the finite-difference stencil used, the PMLs, and then introduce the system of algebraic equations. In Section 3 we discuss the modifications of our structured multifrontal solver from scalar equations to the elastic system. In particular, we give the matrix structure under nested dissection and a complexity analysis, and provide estimates on memory requirements. In Section 4 we give numerical estimates of the rank of the dense matrix prior to HSS compression. We also present the performance of our solver for a model problem. In Section 5 we present various numerical experiments: (i) multi-frequency shear-wave splitting and a comparison with a time-domain discontinuous Galerkin method, (ii) the formation of caustics in $qSV$-wave constituents , (iii) the presence of conical points and a comparison with a spectral element method, (iv) the focusing and defocusing of displacement in a strongly heterogeneous VTI medium, and (v) the polarization decomposition of the solution. We end with some conclusions.

## 2. Propagation of time-harmonic elastic waves.

**2.1. The system of partial differential equations.** We write $\mathbf{x} = (x_1, x_2, x_3)$. Here 1, 2 and 3 denote the $x$, $y$ and $z$ spatial directions in 3D, respectively. We consider the displacement formulation of the system describing time-harmonic elastic waves, with full anisotropy:

$$-\frac{\partial \sigma_{ij}}{\partial x_j} - \rho\omega^2 u_i = f_i, \quad i,j = 1,2,3; \tag{2.1}$$

$\mathbf{f} = (f_1, f_2, f_3)$ is the forcing term, $\mathbf{u} = (u_1, u_2, u_3)$ is the displacement vector, $\rho$ is the density which depends on $x$, and $\sigma$ is the stress tensor. The constitutive relation between the stress and the strain is given by

$$\begin{pmatrix} \sigma_{11} \\ \sigma_{22} \\ \sigma_{33} \\ \sigma_{23} \\ \sigma_{31} \\ \sigma_{12} \end{pmatrix} = \begin{pmatrix} C_{11} & C_{12} & C_{13} & C_{14} & C_{15} & C_{16} \\ * & C_{22} & C_{23} & C_{24} & C_{25} & C_{26} \\ * & * & C_{33} & C_{34} & C_{35} & C_{36} \\ * & * & * & C_{44} & C_{45} & C_{46} \\ * & * & * & * & C_{55} & C_{56} \\ * & * & * & * & * & C_{66} \end{pmatrix} \begin{pmatrix} \frac{\partial u_1}{\partial x_1} \\ \frac{\partial u_2}{\partial x_2} \\ \frac{\partial u_3}{\partial x_3} \\ \frac{\partial u_2}{\partial x_3} + \frac{\partial u_3}{\partial x_2} \\ \frac{\partial u_3}{\partial x_1} + \frac{\partial u_1}{\partial x_3} \\ \frac{\partial u_1}{\partial x_2} + \frac{\partial u_2}{\partial x_1} \end{pmatrix} \tag{2.2}$$

where $\mathbf{C} = [C_{ij}], i = 1, 2, ..., 6, j = 1, 2, ..., 6$ is the stiffness tensor flattened on a matrix; $*$ indicates the symmetry of $\mathbf{C}$. If we consider the orthorhombic anisotropy, 21 stiffness moduli reduce to 9 independent ones. Then we have

$$\begin{pmatrix} \sigma_{11} \\ \sigma_{22} \\ \sigma_{33} \\ \sigma_{23} \\ \sigma_{31} \\ \sigma_{12} \end{pmatrix} = \begin{pmatrix} C_{11} & C_{12} & C_{13} & 0 & 0 & 0 \\ * & C_{22} & C_{23} & 0 & 0 & 0 \\ * & * & C_{33} & 0 & 0 & 0 \\ * & * & * & C_{44} & 0 & 0 \\ * & * & * & * & C_{55} & 0 \\ * & * & * & * & * & C_{66} \end{pmatrix} \begin{pmatrix} \frac{\partial u_1}{\partial x_1} \\ \frac{\partial u_2}{\partial x_2} \\ \frac{\partial u_3}{\partial x_3} \\ \frac{\partial u_2}{\partial x_3} + \frac{\partial u_3}{\partial x_2} \\ \frac{\partial u_3}{\partial x_1} + \frac{\partial u_1}{\partial x_3} \\ \frac{\partial u_1}{\partial x_2} + \frac{\partial u_2}{\partial x_1} \end{pmatrix}, \tag{2.3}$$

where

$$\begin{aligned} &C_{33} = \rho V_p^2, \qquad C_{22} = C_{33}(1 + 2\epsilon^{(1)}), \qquad C_{11} = C_{33}(1 + 2\epsilon^{(2)}), \\ &C_{55} = \rho V_s^2, \qquad C_{66} = C_{55}(1 + 2\gamma^{(1)}), \qquad C_{44} = \frac{C_{66}}{1 + 2\gamma^{(2)}}, \\ &C_{23} = (C_{33} - C_{44})\sqrt{1 + \frac{2\delta^{(1)}}{1 - C_{44}/C_{33}}} - C_{44}, \\ &C_{13} = (C_{33} - C_{55})\sqrt{1 + \frac{2\delta^{(2)}}{1 - C_{55}/C_{33}}} - C_{55}, \\ &C_{12} = (C_{11} - C_{66})\sqrt{1 + \frac{2\delta^{(3)}}{1 - C_{66}/C_{11}}} - C_{66}. \end{aligned}$$

Here $V_p$ represents the "vertical" $P$-wave velocity, and $V_s$ is the "vertical" $S$-wave velocity, and $\epsilon^{(1)}$, $\epsilon^{(2)}$, $\delta^{(1)}$, $\delta^{(2)}$, $\delta^{(3)}$, $\gamma^{(1)}$ and $\gamma^{(2)}$ are the extended Thomsen's parameters for orthorhombic media introduced by [19]. We note that if $\epsilon = \epsilon^{(1)} = \epsilon^{(2)}$, $\delta = \delta^{(1)} = \delta^{(2)} = \delta^{(3)}$ and $\gamma = \gamma^{(1)} = \gamma^{(2)}$, the orthorhombic anisotropy expressed by equation (2.3) reduces to TI (Transverse Isotropy) anisotropy; $\epsilon$, $\delta$ and $\gamma$ are conventional Thomsen's parameters introduced by [17].

After substituting equation (2.2) into equation (2.1), we obtain the following coupled system of equations,

$$\left[\mathbf{A}(\mathbf{x}, \partial_{\mathbf{x}}, \omega) - \rho\omega^2 \mathbf{I}\right] \mathbf{u}(\mathbf{x}, \omega) = \mathbf{f}(\mathbf{x}, \omega) \tag{2.4}$$

or

$$\begin{pmatrix} A_{11} - \rho\omega^2 & A_{12} & A_{13} \\ A_{21} & A_{22} - \rho\omega^2 & A_{23} \\ A_{31} & A_{32} & A_{33} - \rho\omega^2 \end{pmatrix} \begin{pmatrix} u_1 \\ u_2 \\ u_3 \end{pmatrix} = \begin{pmatrix} f_1 \\ f_2 \\ f_3 \end{pmatrix}, \tag{2.5}$$

in which each element $A_{ij} (i = 1, 2, 3, j = 1, 2, 3)$ of $\mathbf{A}(\mathbf{x}, \partial_{\mathbf{x}}, \omega)$ is a second-order partial differential

operator. For example,

$$\begin{aligned}A_{11} =& -\frac{\partial}{\partial x_1}\left(C_{11}\frac{\partial}{\partial x_1}\right)-\frac{\partial}{\partial x_1}\left(C_{16}\frac{\partial}{\partial x_2}\right)-\frac{\partial}{\partial x_1}\left(C_{15}\frac{\partial}{\partial x_3}\right)\\ &-\frac{\partial}{\partial x_2}\left(C_{16}\frac{\partial}{\partial x_1}\right)-\frac{\partial}{\partial x_2}\left(C_{66}\frac{\partial}{\partial x_2}\right)-\frac{\partial}{\partial x_2}\left(C_{56}\frac{\partial}{\partial x_3}\right)\\ &-\frac{\partial}{\partial x_3}\left(C_{15}\frac{\partial}{\partial x_1}\right)-\frac{\partial}{\partial x_3}\left(C_{56}\frac{\partial}{\partial x_2}\right)-\frac{\partial}{\partial x_3}\left(C_{55}\frac{\partial}{\partial x_3}\right),\end{aligned}$$

which reduces to

$$A_{11} = -\frac{\partial}{\partial x_1}\left(C_{11}\frac{\partial}{\partial x_1}\right)-\frac{\partial}{\partial x_2}\left(C_{66}\frac{\partial}{\partial x_2}\right)-\frac{\partial}{\partial x_3}\left(C_{55}\frac{\partial}{\partial x_3}\right)$$

in the orthorhombic case.

**2.2. The system of algebraic equations.** As in the work of [14], we use a 27-point finite difference stencil, the structure of which is illustrated in Figure 1, together with the mass lumping technique and convolutional PML boundary conditions, to discretize equation (2.5) in orthorhombic media. The resulting discretization of $\mathbf{A}(\mathbf{x},\partial_{\mathbf{x}},\omega)$ is denoted as $\widehat{\mathbf{A}}(\mathbf{x},\omega)$. The motivation of using a 27-point stencil is is to improve the shape of the slowness surface associated with the finite difference approximation with additional degrees of freedom within the orthorhombic symmetry. This leads to the following grouping of grid points:

$$\begin{aligned}&\widehat{\mathbf{A}} = w_{s1}\mathbf{A}^{(c)}+\frac{w_{s2}}{3}\left(\mathbf{A}^{(x)}+\mathbf{A}^{(y)}+\mathbf{A}^{(z)}\right)+\frac{w_{s3}}{4}\left(\mathbf{A}^{(1)}+\mathbf{A}^{(2)}+\mathbf{A}^{(3)}+\mathbf{A}^{(4)}\right),\\ &w_{s1}+w_{s2}+w_{s3}=1,\end{aligned}\tag{2.6}$$

where we optimize for $w_{s1}$, $w_{s2}$ and $w_{s3}$; $\mathbf{A}^{(c)}$, $\mathbf{A}^{(x)}$, $\mathbf{A}^{(y)}$, $\mathbf{A}^{(z)}$, $\mathbf{A}^{(1)}$, $\mathbf{A}^{(2)}$, $\mathbf{A}^{(3)}$ and $\mathbf{A}^{(4)}$ are different groupings of grid points based on the orthorhombic symmetry, illustrated in Figure 1. In Appendix A, we give an example of the complete evaluation of one entry $\widehat{A}_{11}(\mathbf{x},\omega)$ for orthorhombic media.

To evaluate the diagonal term $\rho\omega^2\mathbf{u}$, we define the mass lumping operator $\mathbf{M}$,

$$\begin{aligned}&\mathbf{M}\mathbf{u} = w_{m1}\left[\rho\mathbf{u}\right]_1+\frac{w_{m2}}{6}\left[\rho\mathbf{u}\right]_2+\frac{w_{m3}}{12}\left[\rho\mathbf{u}\right]_3+\frac{w_{m4}}{8}\left[\rho\mathbf{u}\right]_4,\\ &w_{m1}+w_{m2}+w_{m3}+w_{m4}=1,\end{aligned}\tag{2.7}$$

where

$$\begin{aligned}\left[\rho\mathbf{u}\right]_1 =&\rho_{000}\mathbf{u}_{000},\\ \left[\rho\mathbf{u}\right]_2 =&\rho_{-100}\mathbf{u}_{-100}+\rho_{100}\mathbf{u}_{100}+\rho_{0-10}\mathbf{u}_{0-10}+\rho_{010}\mathbf{u}_{010}+\rho_{00-1}\mathbf{u}_{00-1}+\rho_{001}\mathbf{u}_{001},\\ \left[\rho\mathbf{u}\right]_3 =&\rho_{-1-10}\mathbf{u}_{-1-10}+\rho_{1-10}\mathbf{u}_{1-10}+\rho_{-110}\mathbf{u}_{-110}+\rho_{110}\mathbf{u}_{110}+\rho_{0-1-1}\mathbf{u}_{0-1-1}+\rho_{01-1}\mathbf{u}_{01-1}\\ &+\rho_{0-11}\mathbf{u}_{0-11}+\rho_{011}\mathbf{u}_{011}+\rho_{-10-1}\mathbf{u}_{-10-1}+\rho_{10-1}\mathbf{u}_{10-1}+\rho_{-101}\mathbf{u}_{-101}+\rho_{101}\mathbf{u}_{101},\\ \left[\rho\mathbf{u}\right]_4 =&\rho_{-1-1-1}\mathbf{u}_{-1-1-1}+\rho_{111}\mathbf{u}_{111}+\rho_{-111}\mathbf{u}_{-111}+\rho_{1-11}\mathbf{u}_{1-11}\\ &+\rho_{11-1}\mathbf{u}_{11-1}+\rho_{-1-11}\mathbf{u}_{-1-11}+\rho_{1-1-1}\mathbf{u}_{1-1-1}+\rho_{-11-1}\mathbf{u}_{-11-1}.\end{aligned}$$

Here, the subscripts of $\rho$ and $\mathbf{u}$ represent different points in the 27-point stencil illustrated in Figure 1. $w_{m1}$, $w_{m2}$, $w_{m3}$ and $w_{m4}$ are weights to be determined. We summarize the discrete system of equation (2.5) into the following equation:

$$\left[\widehat{\mathbf{A}}(\mathbf{x},\omega)-\omega^2\mathbf{M}(\mathbf{x})\right]\mathbf{u}(.,\omega)=\mathbf{f}(\mathbf{x},\omega)\tag{2.8}$$

The conversion from subscripts to a linear index is chosen to be ($D=3$):

$$\begin{aligned}&\mathsf{u}_{(k-1)N_1N_2 3+(j-1)N_1 3+(i-1)3+d} = u_d(x_{1,i},x_{2,j},x_{3,k},\omega),\\ &d=1,\ldots,3,\ i=1,\ldots,N_1,\ j=1,\ldots,N_2,\ k=1,\ldots,N_3.\end{aligned}$$

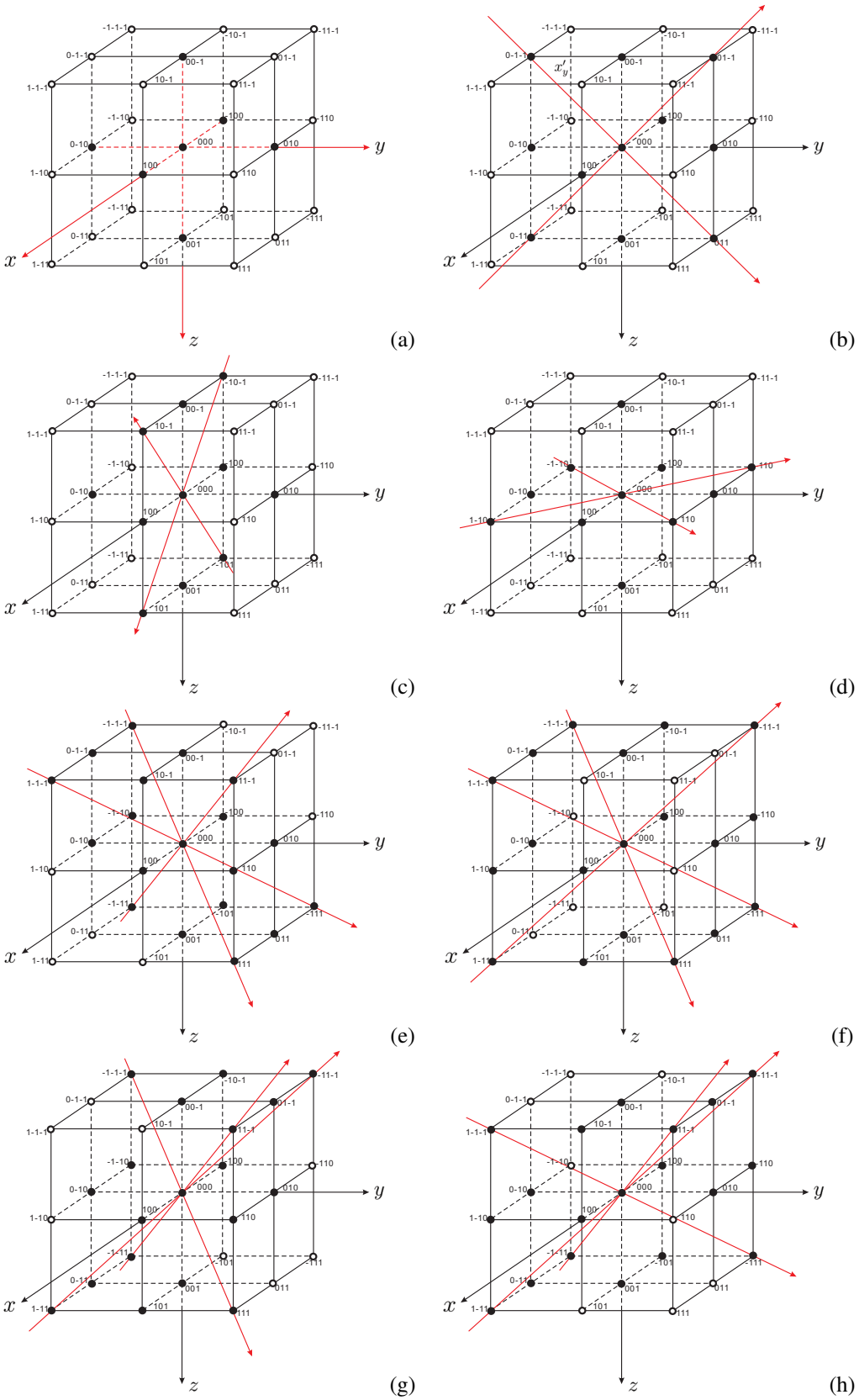


FIG. 1. *Groupings of points (equation (2.6)) in the 27-point finite difference stencil; solid balls indicate points that are included in the component stencil and circles indicate those that are not included; (a):* $\mathbf{A}^{(c)}$*; (b):* $\mathbf{A}^{(x)}$*; (c):* $\mathbf{A}^{(y)}$*; (d):* $\mathbf{A}^{(z)}$*; (e):* $\mathbf{A}^{(1)}$*; (f):* $\mathbf{A}^{(2)}$*; (g):* $\mathbf{A}^{(3)}$*; (h):* $\mathbf{A}^{(4)}$.

The implied matrix, denoted by $\mathsf{A}(\omega)$, is of size $(3N_1N_2N_3) \times (3N_1N_2N_3)$, and shares the same non-zero pattern for different $\omega$. The matrix is pattern symmetric, non-Hermitian, indefinite and ill-conditioned. We set $n = 3N_1N_2N_3$. The body force, upon sampling, takes the form

$$\mathsf{f}_{(k-1)N_1N_2 3+(j-1)N_1 3+(i-1)3+d} = f_d(x_{1,i}, x_{2,j}, x_{3,k}, \omega),$$
$$d = 1, \ldots, 3,\ i = 1, \ldots, N_1,\ j = 1, \ldots, N_2,\ k = 1, \ldots, N_3.$$

We end up with the a linear system of equations,

$$\mathsf{A}(\omega)\ \mathsf{u}(\omega) = \mathsf{f}(\omega), \tag{2.9}$$

where, by abuse of notation, $\mathsf{A}(\omega)$ contains the contributions both from $\widehat{\mathbf{A}}$ and $-\omega^2\mathbf{M}$. The seismic sources $\mathsf{f}(\omega)$ we consider are exploding point sources, and body forces. We use a sharp Gaussian function as a regularized point source.

**2.3. Numerical dispersion analysis.** We present a classical numerical dispersion analysis of our finite difference discretization, and show that with only 5 grid points per shear wavelength, we can achieve reasonable accuracy. We follow the work of [11], [20], [6], and [14]. We consider a Fourier component, $\mathbf{u} = \mathbf{u}_0 \exp(-\mathrm{i}\mathbf{k}\cdot\mathbf{x})$, where $\mathbf{k}$ is a wave vector and $\mathbf{u}_0$ is a polarization vector. The phase velocity is given by $V_{ph} = \omega/|\mathbf{k}|$. In polar coordinates, we write

$$\mathbf{k}\cdot\mathbf{x} = \frac{2\pi}{G}\left(r\cos\theta\cos\varphi + s\cos\theta\sin\varphi + t\sin\theta\right), \tag{2.10}$$

where $(r, s, t)$ are the spatial coordinates and $G$ signifies the number of grid points per wavelength. We cast our dispersion analysis in the framework of 3D orthorhombic media:

$$\det\left[\frac{1}{|\mathbf{k}|^2}\exp(\mathrm{i}\mathbf{k}\cdot\mathbf{x})\mathbf{M}^{-1}\widehat{\mathbf{A}}\exp(-\mathrm{i}\mathbf{k}\cdot\mathbf{x}) - V_{ph}^2\mathbf{I}\right] = 0. \tag{2.11}$$

We write $\mathbf{B} = \frac{1}{|\mathbf{k}|^2}\exp(\mathrm{i}\mathbf{k}\cdot\mathbf{x})\mathbf{M}^{-1}\widehat{\mathbf{A}}\exp(-\mathrm{i}\mathbf{k}\cdot\mathbf{x})$, with elements

$$B_{11} = \frac{C_{11}E_{xx} + C_{66}E_{yy} + C_{55}E_{zz}}{\rho J\left(\frac{2\pi}{G}\right)^2},$$
$$B_{22} = \frac{C_{66}E_{xx} + C_{22}E_{yy} + C_{44}E_{zz}}{\rho J\left(\frac{2\pi}{G}\right)^2},$$
$$B_{33} = \frac{C_{55}E_{xx} + C_{44}E_{yy} + C_{33}E_{zz}}{\rho J\left(\frac{2\pi}{G}\right)^2},$$
$$B_{12} = B_{21} = \frac{(C_{12} + C_{66})\,E_{xy}}{\rho J\left(\frac{2\pi}{G}\right)^2},$$
$$B_{23} = B_{32} = \frac{(C_{23} + C_{44})\,E_{yz}}{\rho J\left(\frac{2\pi}{G}\right)^2},$$
$$B_{13} = B_{31} = \frac{(C_{13} + C_{55})\,E_{zx}}{\rho J\left(\frac{2\pi}{G}\right)^2},$$

where

$$
\begin{aligned}
E_{xx} &= 2(1-\cos a)\left[w_{s1} + \frac{4+\cos b+\cos c}{6} w_{s2} + \frac{1+\cos b\cos c}{2} w_{s3}\right],\\
E_{yy} &= 2(1-\cos b)\left[w_{s1} + \frac{4+\cos c+\cos a}{6} w_{s2} + \frac{1+\cos c\cos a}{2} w_{s3}\right],\\
E_{zz} &= 2(1-\cos c)\left[w_{s1} + \frac{4+\cos a+\cos b}{6} w_{s2} + \frac{1+\cos a\cos b}{2} w_{s3}\right],\\
E_{xy} &= \sin a \sin b\left[w_{s1} + \frac{1+2\cos c}{3} w_{s2} + (2-\cos a\cos b\cos c) w_{s3}\right],\\
E_{yz} &= \sin b \sin c\left[w_{s1} + \frac{1+2\cos a}{3} w_{s2} + (2-\cos a\cos b\cos c) w_{s3}\right],\\
E_{zx} &= \sin c \sin a\left[w_{s1} + \frac{1+2\cos b}{3} w_{s2} + (2-\cos a\cos b\cos c) w_{s3}\right]
\end{aligned}
$$

and

$$
\begin{aligned}
&a = \frac{2\pi}{G}\cos\theta\cos\varphi, \quad b = \frac{2\pi}{G}\cos\theta\sin\varphi, \quad c = \frac{2\pi}{G}\sin\theta,\\
&\alpha = \cos a + \cos b + \cos c,\\
&\beta = \cos a\cos b + \cos b\cos c + \cos c\cos a,\\
&\eta = \cos a\cos b\cos c,\\
&J = w_{m1} + \frac{w_{m2}}{3}\alpha + \frac{w_{m3}}{3}\beta + w_{m4}\eta.
\end{aligned}
$$

We compare the solutions with the solutions of

$$
\det\left[\frac{\mathbf{A}(\mathbf{x},\mathbf{k},\omega)}{\rho|\mathbf{k}|^2} - \widetilde{V}_{ph}^2\mathbf{I}\right] = 0, \tag{2.12}
$$

where $\widetilde{V}_{ph}$ denotes exact phase velocities, and

$$
\begin{aligned}
\left(\rho^{-1}|\mathbf{k}|^{-2}\mathbf{A}(\mathbf{x},\mathbf{k},\omega)\right)_{11} &= \frac{C_{11}}{\rho}(\cos\theta\cos\varphi)^2 + \frac{C_{66}}{\rho}(\cos\theta\sin\varphi)^2 + \frac{C_{55}}{\rho}(\sin\theta)^2,\\
\left(\rho^{-1}|\mathbf{k}|^{-2}\mathbf{A}(\mathbf{x},\mathbf{k},\omega)\right)_{22} &= \frac{C_{66}}{\rho}(\cos\theta\cos\varphi)^2 + \frac{C_{22}}{\rho}(\cos\theta\sin\varphi)^2 + \frac{C_{44}}{\rho}(\sin\theta)^2,\\
\left(\rho^{-1}|\mathbf{k}|^{-2}\mathbf{A}(\mathbf{x},\mathbf{k},\omega)\right)_{33} &= \frac{C_{55}}{\rho}(\cos\theta\cos\varphi)^2 + \frac{C_{44}}{\rho}(\cos\theta\sin\varphi)^2 + \frac{C_{33}}{\rho}(\sin\theta)^2,\\
\left(\rho^{-1}|\mathbf{k}|^{-2}\mathbf{A}(\mathbf{x},\mathbf{k},\omega)\right)_{12} &= \left(\rho^{-1}|\mathbf{k}|^{-2}\mathbf{A}(\mathbf{x},\mathbf{k},\omega)\right)_{21} = \frac{C_{12}+C_{66}}{\rho}\cos^2\theta\sin\varphi\cos\varphi,\\
\left(\rho^{-1}|\mathbf{k}|^{-2}\mathbf{A}(\mathbf{x},\mathbf{k},\omega)\right)_{23} &= \left(\rho^{-1}|\mathbf{k}|^{-2}\mathbf{A}(\mathbf{x},\mathbf{k},\omega)\right)_{32} = \frac{C_{23}+C_{44}}{\rho}\sin\theta\cos\theta\sin\varphi,\\
\left(\rho^{-1}|\mathbf{k}|^{-2}\mathbf{A}(\mathbf{x},\mathbf{k},\omega)\right)_{13} &= \left(\rho^{-1}|\mathbf{k}|^{-2}\mathbf{A}(\mathbf{x},\mathbf{k},\omega)\right)_{31} = \frac{C_{13}+C_{55}}{\rho}\sin\theta\cos\theta\cos\varphi.
\end{aligned}
$$

As an example, we compute phase velocities in an orthorhombic model described in Figure 2, with respect to the full range of $1/G = [0.01, 0.3]$, $\theta = [0, \pi]$ and $\phi = [0, \pi]$. The weights are found to be $w_{s1} = 0.2$, $w_{s2} = 0.6$, $w_{s3} = 0.2$; $w_{m1} = 0.5$, $w_{m2} = 0.45$, $w_{m3} = 0.05$, $w_{m4} = 0.0$. In row one, we solve equation (2.12) and obtain three theoretical phase velocities for $qP$, $qS1$ and $qS2$ modes. Then we solve the equation (2.11) with $G = 5$. Row two and three display results for classical second order centered finite difference without mass lumping and the mixed grid finite difference with mass lumping,

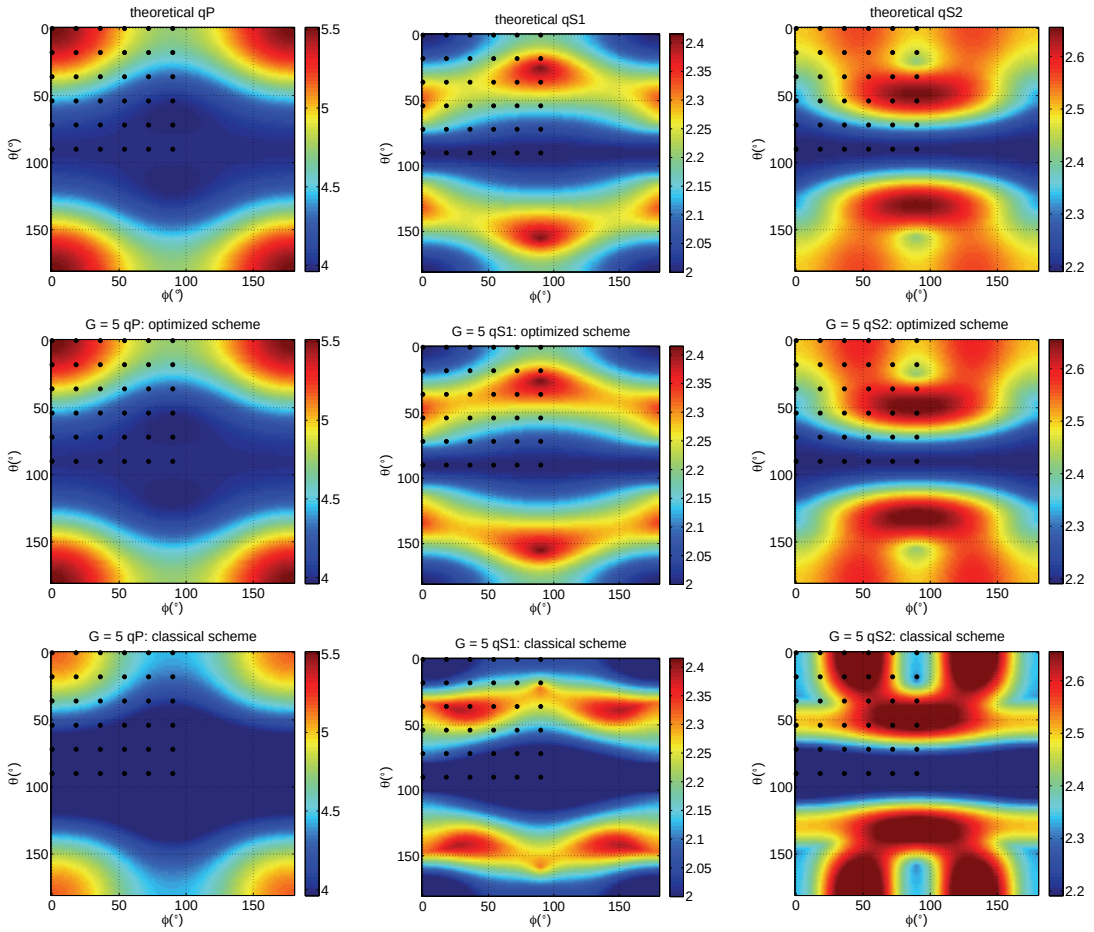


FIG. 2. *Phase velocities for the orthorhombic model:* $V_p = 4000$*m/s,* $V_s = 2000$*m/s,* $\rho = 1.0$*,* $\epsilon^{(1)} = 0.2$*,* $\epsilon^{(2)} = 0.45$*,* $\delta^{(1)} = -0.1$*,* $\delta^{(2)} = 0.2$*,* $\delta^{(3)} = -0.15$*,* $\gamma^{(1)} = 0.28$*,* $\gamma^{(2)} = 0.15$*;* ***row one****: theoretical phase velocities;* ***row two****: numerical phase velocities for* $G = 5$ *using the mixed finite difference scheme with mass lumping;* ***row three****: numerical phase velocities for* $G = 5$ *using the classical second order centered finite difference scheme without mass lumping;* ***column one****: phase velocities for* $qP$*;* ***column two****: phase velocities for* $qS1$*;* ***column three****: phase velocities for* $qS2$*.*

respectively. The three columns display phase velocities for $qP$, $qS1$ and $qS2$, respectively. We present normalized phase velocities $V_{ph}/\widetilde{V}_{ph}$ with respect to $1/G$ in Figure 3, for angles indicated by solid dots in Figure 2. Row one and two display results for the second-order centered finite difference and the optimized finite difference approximation, respectively. Column one to three display the phase velocities for $qP$, $qS1$ and $qS2$, respectively. We observe that 5 grid point per shear wavelength allow us to conduct modeling with reasonable accuracy.

**3. Nested dissection and the multifrontal method for the elastic system of equations.** In this section, we give a brief overview of the structured multifrontal solver together with the nested dissection based domain decomposition techniques introduced by [22] and [24], for modeling time-harmonic waves in (anisotropic) acoustic media. Then we study in detail similarities and differences between the acoustic and the elastic modeling, via the same structured multifrontal factorization approach. Eventually we present comparisons of both computational complexity and storage between the acoustic and elastic modeling, for the same problem size.

**3.1. Overview of the structured multifrontal solver.** To solve the acoustic analog matrix system of equation (cf. (2.9)), [22] introduced a massively parallel structured multifrontal solver together with the

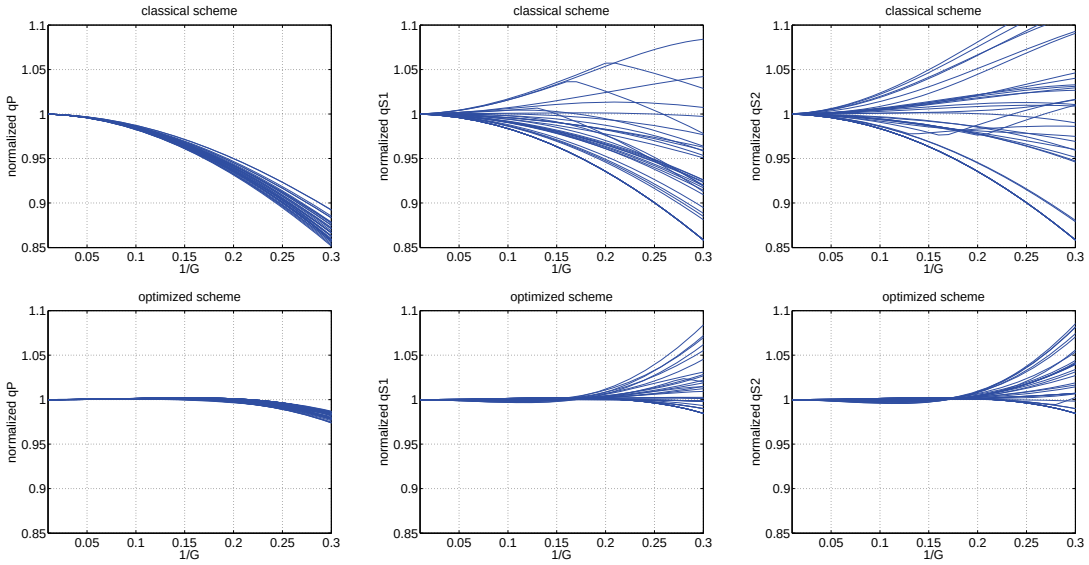


FIG. 3. *Dispersion curves for the orthorhombic model and angles indicated by dots in Figure 2;* ***row one****: the classical second order centered finite difference scheme without mass lumping;* ***row two****: the mixed finite difference scheme with mass lumping;* ***column one****: $qP$ dispersion curves;* ***column two****: $qS1$ dispersion curves;* ***column three****: $qS2$ dispersion curves.*

nested dissection based domain decomposition, imbedding a scalable Hierarchically SemiSeparable (HSS) matrix solver. They showed that, in 3D, the computational complexity associated with the factorization is between $\mathcal{O}(n \log n)$ and $\mathcal{O}(n^{4/3} \log n)$, and storage is between $\mathcal{O}(n)$ and $\mathcal{O}(n \log n)$, reminding that $n$ denotes the size of the matrix $\mathsf{A}(\omega)$.

They first conduct the nested dissection reordering (see [10]) of $\mathsf{A}(\omega)$ by dividing upper level domains into lower level subdomains and separators recursively, imposing that the mesh points associated with subdomains are reordered prior to ones associated with separators, and lower level domains are reordered prior to the upper level ones. This yields a post-ordering tree structure named *assembly tree*. The nested dissection reordering, which essentially can be viewed as hierarchical domain decompositions, has been proven to be the optimal reordering strategy that minimizes the fill-in of the factorization. Furthermore, to account for the anisotropy and variable order of accuracy, [24] extended the nested dissection to incorporate separators of variable thickness.

Secondly, after the nested dissection reordering, [22] carry out local partial $LU$ factorizations upon the reordered matrix, via forming *frontal matrices* $\mathsf{F}_i$ and computing *update matrices* $\mathsf{U}_i$ locally on each node $i$ of the assembly tree, by taking advantage of the multifrontal method introduced by [13]. We summarize the mathematics of the multifrontal method in the concise way below:

$$\mathsf{F}_i = \begin{pmatrix} \mathsf{F}_{i,11} & \mathsf{F}_{i,12} \\ \mathsf{F}_{i,21} & \mathsf{F}_{i,22} \end{pmatrix} = \begin{cases} \begin{pmatrix} \mathsf{A}_{i,11} & \mathsf{A}_{i,12} \\ \mathsf{A}_{i,21} & 0 \end{pmatrix}, & \text{if } i \text{ is a leaf node;} \\ \begin{pmatrix} \mathsf{A}_{i,11} & \mathsf{A}_{i,12} \\ \mathsf{A}_{i,21} & 0 \end{pmatrix} + (\mathsf{U}_{c_1} \Diamond \mathsf{U}_{c_2}), & \text{if } i \text{ is a non-leaf node;} \end{cases} \tag{3.1}$$

$$\mathsf{U}_i = \mathsf{F}_{i,22} - \mathsf{F}_{i,21}\, \mathsf{F}_{i,11}^{-1}\, \mathsf{F}_{i,12};$$

where $\mathsf{A}_i$ denotes the portion of the global matrix $\mathsf{A}(\omega)$ associated with the node $i$ on the assembly tree; $c_1$ and $c_2$ are two children of the node $i$ if $i$ is a non-leaf, satisfying $c_1 < c_2 < i$. The extend-add operation is denoted by $\Diamond$. Figure 4 illustrates the multifrontal process associated with the node $i$ on the assembly tree.

Thirdly, by exploiting low rank properties of off-diagonal blocks of frontal matrices $\mathsf{F}_i$, [23] proposed a series of parallel HSS compression, $ULV$ factorization and solution techniques. They show that with the aid of HSS implementations, the cost of factorization of each frontal matrix is reduced from $\mathcal{O}(n_i^3)$ to $\mathcal{O}(r_i n_i^2)$,

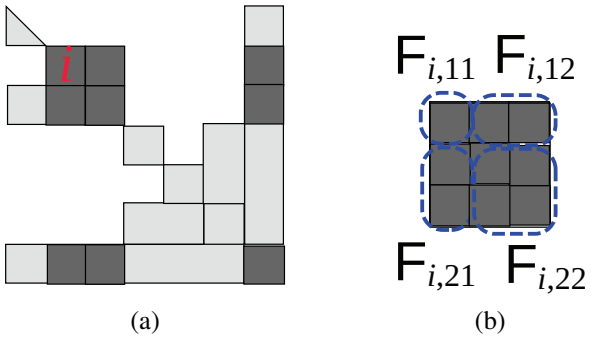


FIG. 4. *The illustration of the multifrontal method summarized in equation (3.1): (a) the multifrontal factorization stage associated with the node $i$; (b) the formation of the frontal matrix $\mathsf{F}_i$.*

as well as the storage is reduced from $\mathcal{O}(n_i^2)$ to $\mathcal{O}(r_i n_i)$, where $n_i$ denotes the size of each frontal matrix $\mathsf{F}_i$, and $r_i$ denotes the maximum numerical rank of all off-diagonal blocks associated with each $\mathsf{F}_i$.

**3.2. Similarities and differences: acoustic v.s. elastic.** We point out that a big difference between the acoustic modeling and the elastic modeling for the same problem size $N_1 \times N_2 \times N_3$ lies in that the number of unknowns for the elastic system is $3N_1N_2N_3$, which is exactly 3 times as large as the number of unknowns for the acoustic system. This is obviously due to the fact that there are 3 components associated with each mesh point for the elastic system rather than only one component that is for the acoustic system. This implies that the size of the elastic matrix $\mathsf{A}(\omega)$ is 3 times as large as the size of the acoustic matrix.

On the other hand, we assume that the thickness of the separators for both the acoustic and elastic systems is $t$, which yields that the number of mesh points for the finite difference stencil associated with the acoustic system is $(2t+1)^3$, while the one for the elastic system finite difference stencil is $3\,(2t+1)^3$. For example, for the acoustic system [22] utilize a 27-point stencil ($t = 1$), which corresponds with an 81-point stencil in the elastic case.

Because both the acoustic system and the elastic system share the same problem size $N_1 \times N_2 \times N_3$ and the same thickness of separator $t$, thus they share exactly the same nested dissection strategy, which, in other words, means that positions and sizes associated with subdomains and separators are exactly the same for both acoustic and elastic system. The only difference between two systems is that after nested dissection reordering, the size $n_i$ of each frontal matrix $\mathsf{F}_i$ associated with the elastic system is exactly 3 times as large as each $n_i$ associated with the acoustic system. Figure 5 illustrates matrix patterns for both acoustic and elastic systems discretized on the same $4 \times 4 \times 4$ mesh, for various levels of nested dissection reordering. We note the similarity of matrix patterns, and the size difference of each matrix block by a factor of 3.

Without resorting to the HSS compression and factorization techniques, we can straightforwardly conclude that the computational complexity for the elastic matrix factorization is $3^3$ times larger than the one associated with the acoustic system, and the storage for the elastic system is $3^2$ times larger than the one for the acoustic system. This is due to the well known fact that the cost of exact $LU$ factorization of each dense frontal matrix $\mathsf{F}_i$ is $\mathcal{O}(n_i^3)$, and the storage is $\mathcal{O}(n_i^2)$. By virtue of HSS low rank compression techniques, the complexity and storage are of the order $\mathcal{O}(r_i n_i^2)$ and $\mathcal{O}(r_i n_i)$, respectively. This brings the complexity ratio from $3^3$ to $3^2$, and the storage ratio from $3^2$ to 3, which comprises the main result of this paper.

**4. Performance.** Here, we briefly discuss the complexity of the solver. The solver performs well if the off-diagonal blocks of the frontal matrices $\mathsf{F}_i$ in (3.1) have small numerical ranks. In general, such a requirement is not satisfied for 3D (elastic) problems. However, in [26, 25], it is shown that if the off-diagonal numerical ranks satisfy certain patterns, then these structured solvers can still work well, and the complexity is similar to the case where the ranks are bounded.

For mesh dimensions $N = 25, 50, 100, 150$, we demonstrate the off-diagonal numerical ranks of the largest frontal matrix $\mathsf{F}_i$ that is of order, say $M$. $\mathsf{F}_i$ is hierarchically partitioned into multiple levels following the definition of HSS matrices [28]. The largest level is where there are most subblocks. The maximum

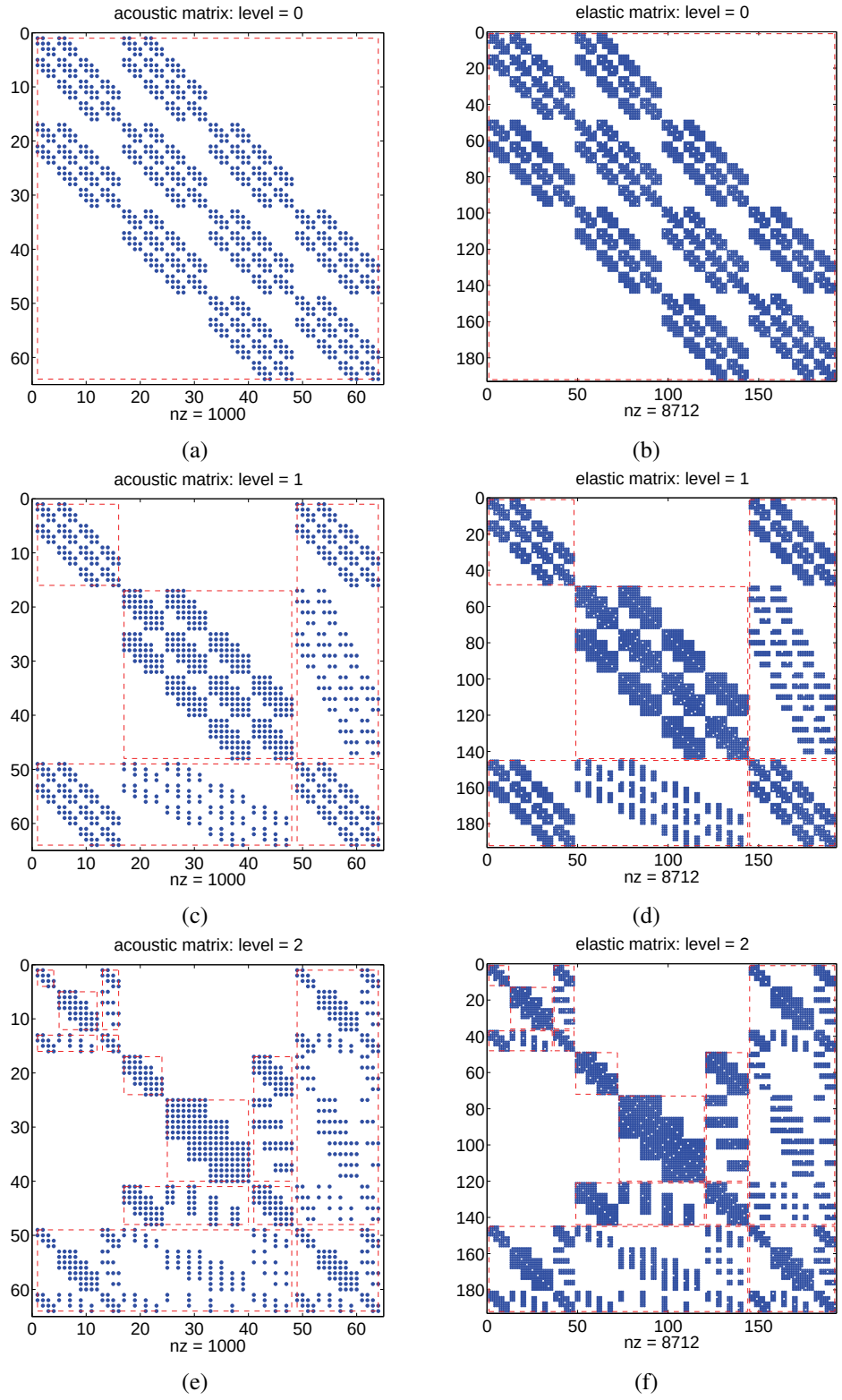


FIG. 5. *The pattern of the matrix* $\mathbf{A}(\omega)$ *discretized on a 3D* $4 \times 4 \times 4$ *mesh. (a): the acoustic matrix without nested dissection; (b): the elastic matrix without nested dissection; (c): the acoustic matrix with one-level nested dissection; (d): the elastic matrix with one-level nested dissection; (e): the acoustic matrix with two-level nested dissection; (f): the elastic matrix with two-level nested dissection.*

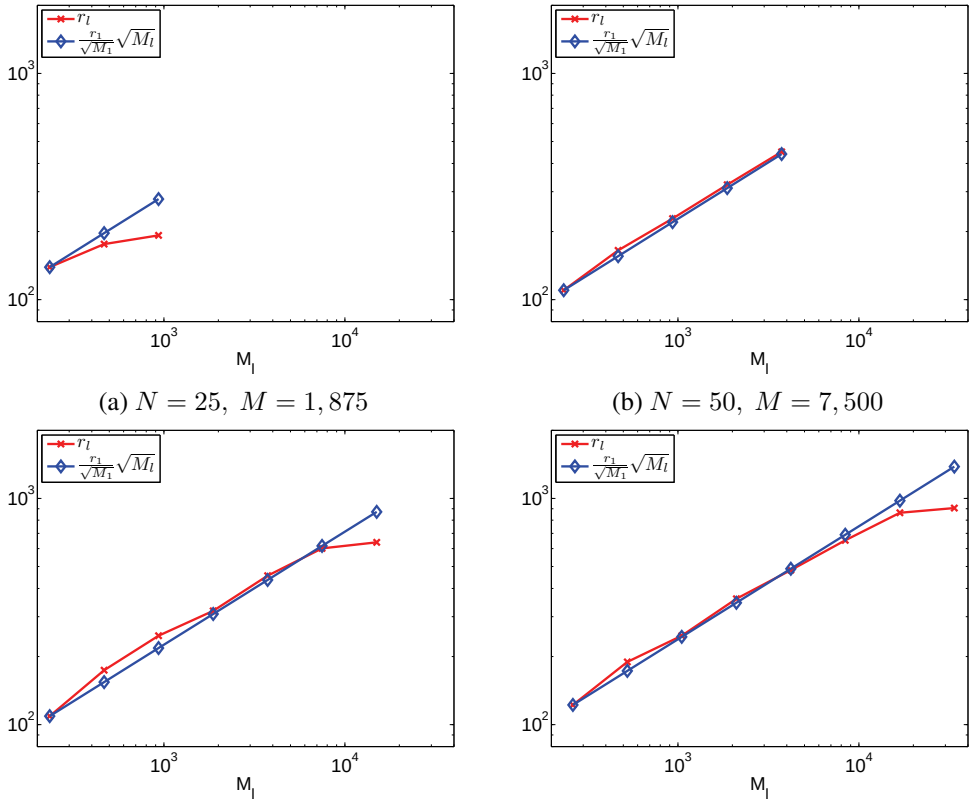


(a) $N = 25,\ M = 1,875$ (b) $N = 50,\ M = 7,500$

(c) $N = 100,\ M = 30,000$ (d) $N = 150,\ M = 67,500$

FIG. 6. *Rank patterns of frontal matrices* $\mathsf{F}_i$ *of order* $M$ *that arises from the factorization of the sparse matrices discretized on* $N \times N \times N$ *meshes.*

numerical rank $r_l$ at each level $l$ of the partition is recorded, and plotted in Figure 6. Although a precise justification is not yet available, these ranks are observed to closely follow the following pattern:

$$r_l = \mathcal{O}\left(\sqrt{M_l}\right),$$

where $M_l$ is the maximum row size of the blocks at level $l$ of the partition. With this pattern, it is shown in [26, 25] that an HSS approximation to $\mathsf{F}_i$ can be constructed in $\xi_0$ flops and factorized in $\xi_1$ flops, where

$$\xi_0 = \mathcal{O}\left(M^2 \log M\right),\ \xi_1 = \mathcal{O}\left(M^{3/2}\right).$$

Moreover, the solution cost is

$$\xi_2 = \mathcal{O}\left(M \log M\right).$$

In contract, the exact factorization and solution costs are $\tilde{\xi}_1 = \mathcal{O}\left(M^3\right)$ and $\tilde{\xi}_2 = \mathcal{O}\left(M^2\right)$, respectively. Notice that when $N$ doubles, $M$ becomes four times larger. Then $\xi_0$, $\xi_1$ and $\xi_2$ increase by factors of 16, 8, and 4, respectively, while $\tilde{\xi}_1$ and $\tilde{\xi}_2$ increase by factors of 64, and 16, respectively. This is illustrated in Figure 7. The overall sparse structured factorization cost is then $O\left(n^{4/3} \log n\right)$, and the solution cost is $O\left(n \log n\right)$, which is nearly linear in $n$ [25].

**5. Numerical experiments.** We present various numerical experiments illustrating the behavior of time-harmonic elastic waves in 3D anisotropic media. Both homogeneous and inhomogeneous 3D models are discretized on a $201 \times 201 \times 151$ mesh, with different step sizes. We set the HSS compression

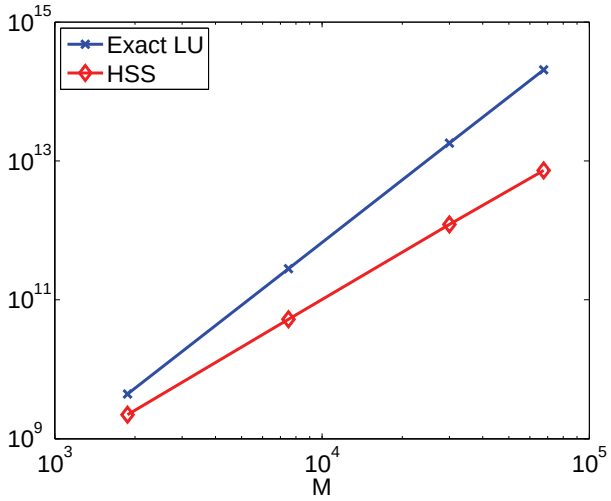


FIG. 7. *HSS construction costs (flops) for the largest frontal matrix* $\mathsf{F}_i$ *of order* $M$ *that arises from the factorization of the sparse matrices discretized on* $N \times N \times N$ *meshes, where* $N = 25, 50, 100, 150$*, with the corresponding* $M = 1875,\ 7500,\ 30000,\ 67500$.

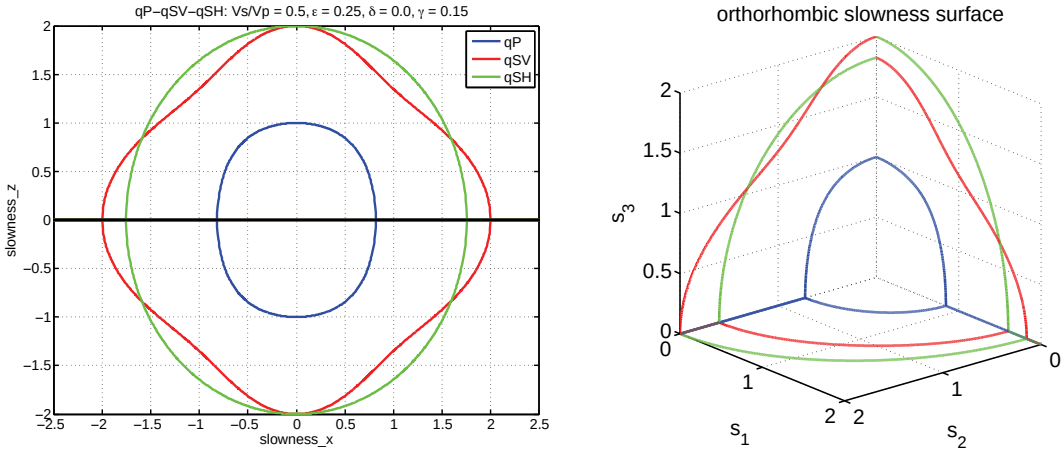


(a) (b)

FIG. 8. *(a): The slowness surfaces of the* $qP$*,* $qSV$ *and* $qSH$ *polarization for the homogeneous elastic VTI model. The parameters of the model are: "vertical" P-wave velocity* $V_p = 4000$*m/s, "vertical" S-wave velocity* $V_s = 2000$*m/s, density* $\rho = 1.0$*, Thomsen's parameters* $\epsilon = 0.25$*,* $\delta = 0.0$*,* $\gamma = 0.15$*; (b): The slowness surfaces of the* $qP$*,* $qS1$ *and* $qS2$ *polarizations for the homogeneous elastic orthorhombic model. The parameters of the model are: "vertical" P-wave velocity* $V_p = 4000$*m/s, "vertical" S-wave velocity* $V_s = 2000$*m/s, density* $\rho = 1.0$*, Thomsen's parameters* $\epsilon^{(1)} = 0.2$*,* $\epsilon^{(2)} = 0.45$*,* $\delta^{(1)} = -0.1$*,* $\delta^{(2)} = 0.2$*,* $\delta^{(3)} = -0.15$*,* $\gamma^{(1)} = 0.28$*,* $\gamma^{(2)} = 0.15$.

threshold to be $1.0e-4$, which results in a four digit accuracy of our computed time-harmonic wavefields. All 3D computations are conducted on a National Energy Research Scientific Computing Center (NERSC) supercomputer named `Hopper.nersc.gov`, utilizing 128 nodes with 16 cores and 32GB of memory per node. The CPU wall time is 2947s, and the total memory consumption is 2316GB.

**5.1. Homogenous media.** Our reference model is depicted by the left slowness surface in Figure 8. Here, we consider a homogeneous medium and different point sources. The system of equations is discretized on a $201 \times 201 \times 151$ mesh with step sizes $h_1 = h_2 = h_3 = 0.035$km, which implies that the model size is $[0, 7]\text{km} \times [0, 7]\text{km} \times [0, 5.25]\text{km}$.

First, we show in Figure 9 a multi-frequency computation and a comparison with a time-domain Dis-

continuous Galerkin method in 2D. The four digit accuracy is sufficient to capture the change of phase in the reverse branch of the triplication. Next, we illustrate the time-harmonic displacement in 3D, in Figure 10, for a vertical point body force. We note the interference between the different polarizations. Our computation has been carried out with a sampling rate of five points per shear wave length. In the $u_3$ component, in the $x_2x_3$ plane, we observe the excitation of $qP$ waves in a cone aligned with the $x_3$ direction and of $qSV$ waves in a cone aligned with the $x_2$ direction, while the presence of a caustic is clear. In the $u_2$ component, in the $x_2x_3$ plane, we observe the $qP$ waves in all directions. Essentially, we observe the imprint of the radiation pattern of the source.

We then consider an orthorhombic model depicted by the right slowness surface in Figure 8. Our computation has been carried out with a sampling rate of five points per shear wave length. We illustrate the time-harmonic displacement generated by an explosive point source in Figure 11 (a)-(c). We note the presence of conical points, for example in the $u_1$ component in the $x_2x_3$ plane. In Figure 11 (d)-(e), we show the wave fronts in the $x_2 = 3.5$km and $x_1 = 5.25$km (symmetry) planes for comparison. The wavefronts both show the formation of caustics and lids associated with the conical points; the locations of such points is illustrated in the $qS1 - qS2$ slowness surfaces presented in Figure 8. The wavefronts aid in clarifying the interference of wave constituents in the Figure 11 (a)-(c).

**5.2. Inhomogeneous medium.** We consider a heterogeneous VTI model, derived from the SEAM3D model, and discretized on a $201 \times 201 \times 151$ mesh with step sizes $h_1 = h_2 = h_3 = 0.022$km that yields the model size $[0, 4.4]\text{km} \times [0, 4.4]\text{km} \times [0, 3.3]\text{km}$. It is illustrated in Figures 12-13. We show the time-harmonic displacement generated by a vertical point body force in Figure 14. This example confirms and illustrates the performance of our algorithm in a salt tectonic geological environment with strong heterogeneities.

Finally, we generate the time-harmonic displacement generated by a vertical point body force in an isotropic heterogeneous model by using the parameters in Figure 12. We decompose the solution into $P$ and $S$ polarizations; the results are shown in Figure 15. The model is smooth and, indeed, the separation is clean.

**6. Conclusion.** We presented a finite-difference modeling algorithm for time-harmonic seismic waves in anisotropic media using locally optimized finite difference stencils. We developed a massively parallel direct structured solver for the relevant system of equations. The system of equations need not be of real principal type. We carried out computational experiments both for TI and orthorhombic media. For fixed frequency, in 3D, the complexity associated with the elastic system is 9 times larger than the one for the acoustic system, and the storage requirement for the elastic modeling is 3 times larger than the one associated with the acoustic modeling. The solver will play a key role in wave-equation tomography and full waveform inversion, and is very well suited for adjoint state computations with a large number of sources (events) potentially on planetary scale.

**7. Acknowledgements.** The authors thank the members, ConocoPhillips, ExxonMobil, PGS, Statoil and Total, , of the Geo-Mathematical Imaging Group (GMIG) for partial financial support. J. Xia was supported in part by NSF grants DMS-1115572 and CHE-0957024, M.V. de Hoop was supported in part by NSF CMG grant DMS-1025318, and X.S. Li was supported in part by the Director, Office of Science, Office of Advanced Scientific Computing Research of the U.S. Department of Energy under the contract DE-AC02-05CH11231. The authors thank the National Energy Research Scientific Computing Center (NERSC) at Lawrence Berkeley National Laboratory (LBNL) for providing the computing resources, and Ruichao Ye for generating time domain multi-component modeling results using the Discontinuous Galerkin method.

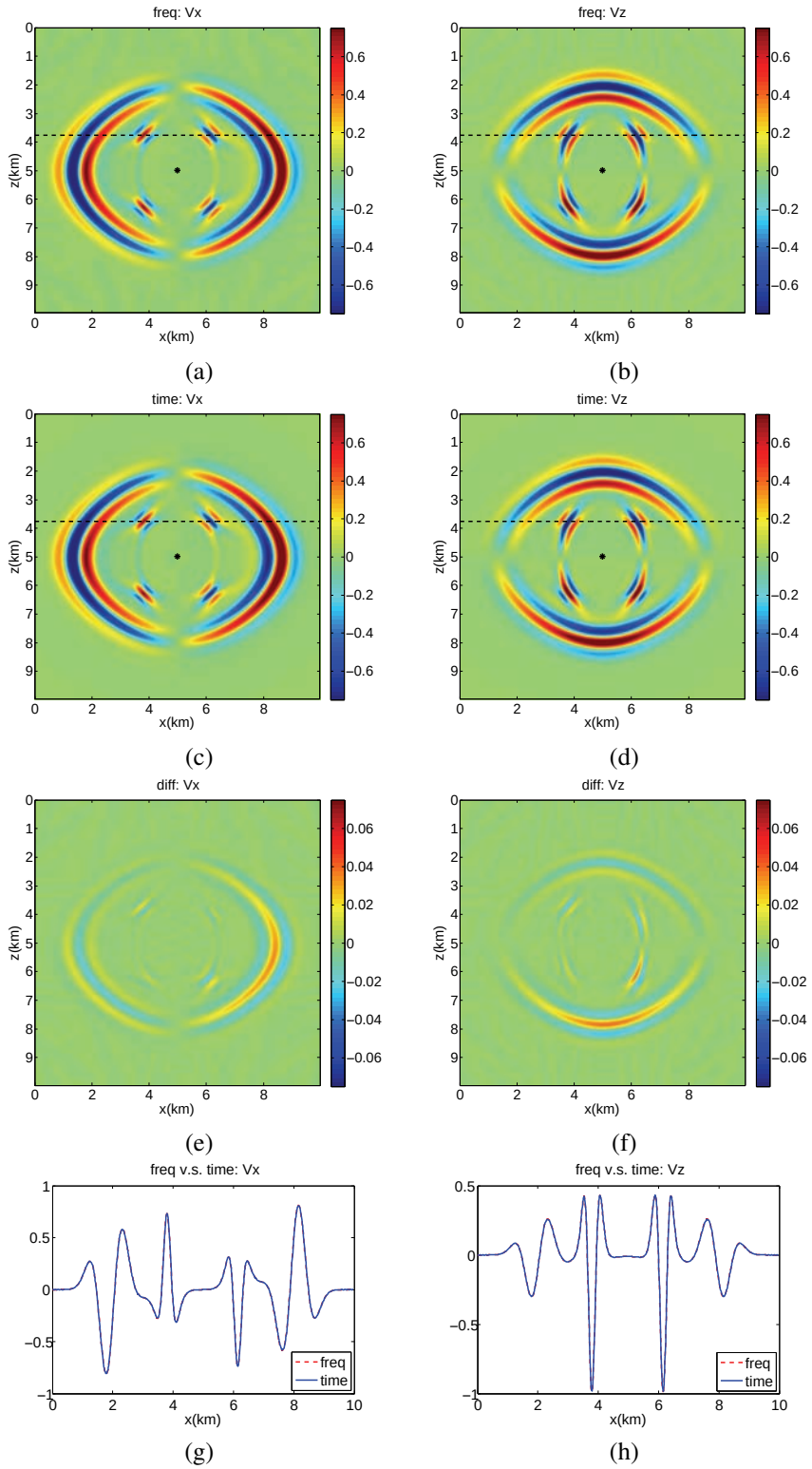


FIG. 9. *A comparison between our frequency domain finite difference multi-component modeling and a multi-component time domain Discontinuous Galerkin method based modeling. (a): $v_1 = \partial_t u_1$ component computed by the frequency domain code; (b): $v_3 = \partial_t u_3$ component computed by the frequency domain code; (c): $v_1$ component computed by the time domain code; (d): $v_3$ component computed by the time domain code; (e): (a)-(c); (f): (b)-(d); (g): a comparison of $v_1$ on the indicated dashed line; (h): a comparison of $v_3$ on the indicated dashed line.*

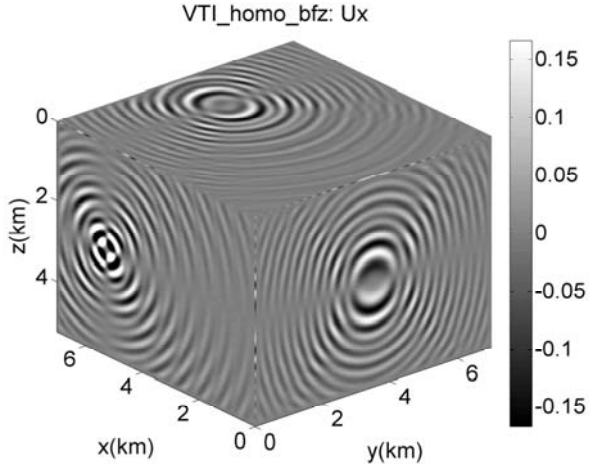


(a)

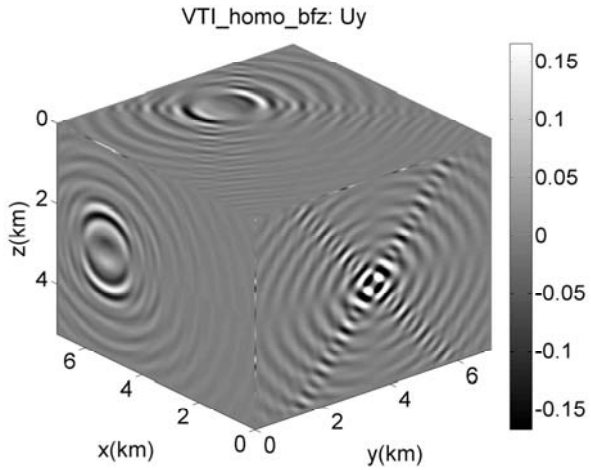


(b)

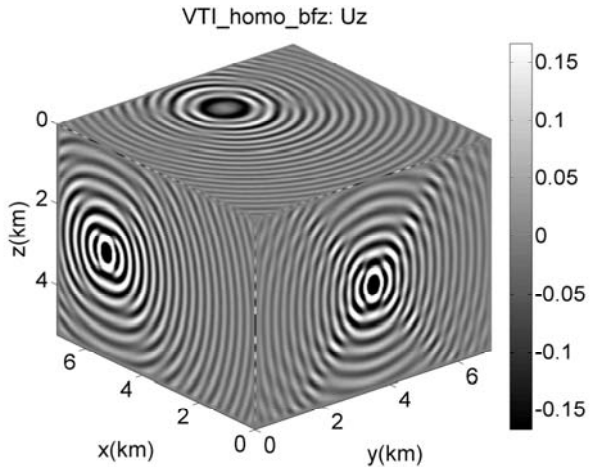


(c)

FIG. 10. *Multi-component time harmonic wavefield generated by a vertical point body force in the homogeneous elastic VTI model depicted in Figure 8. The point body force is located at* $(5.25, 3.5, 2.625)$*km. (a):* $u_1$ *displayed on the planes of* $x_1 = 6.125$*km,* $x_2 = 3.5$*km and* $x_3 = 3.5$*km; (b):* $u_2$ *displayed on the planes of* $x_1 = 5.25$*km,* $x_2 = 4.375$*km and* $x_3 = 3.5$*km; (c):* $u_3$ *displayed on the planes of* $x_1 = 5.25$*km,* $x_2 = 3.5$*km and* $x_3 = 3.5$*km.*

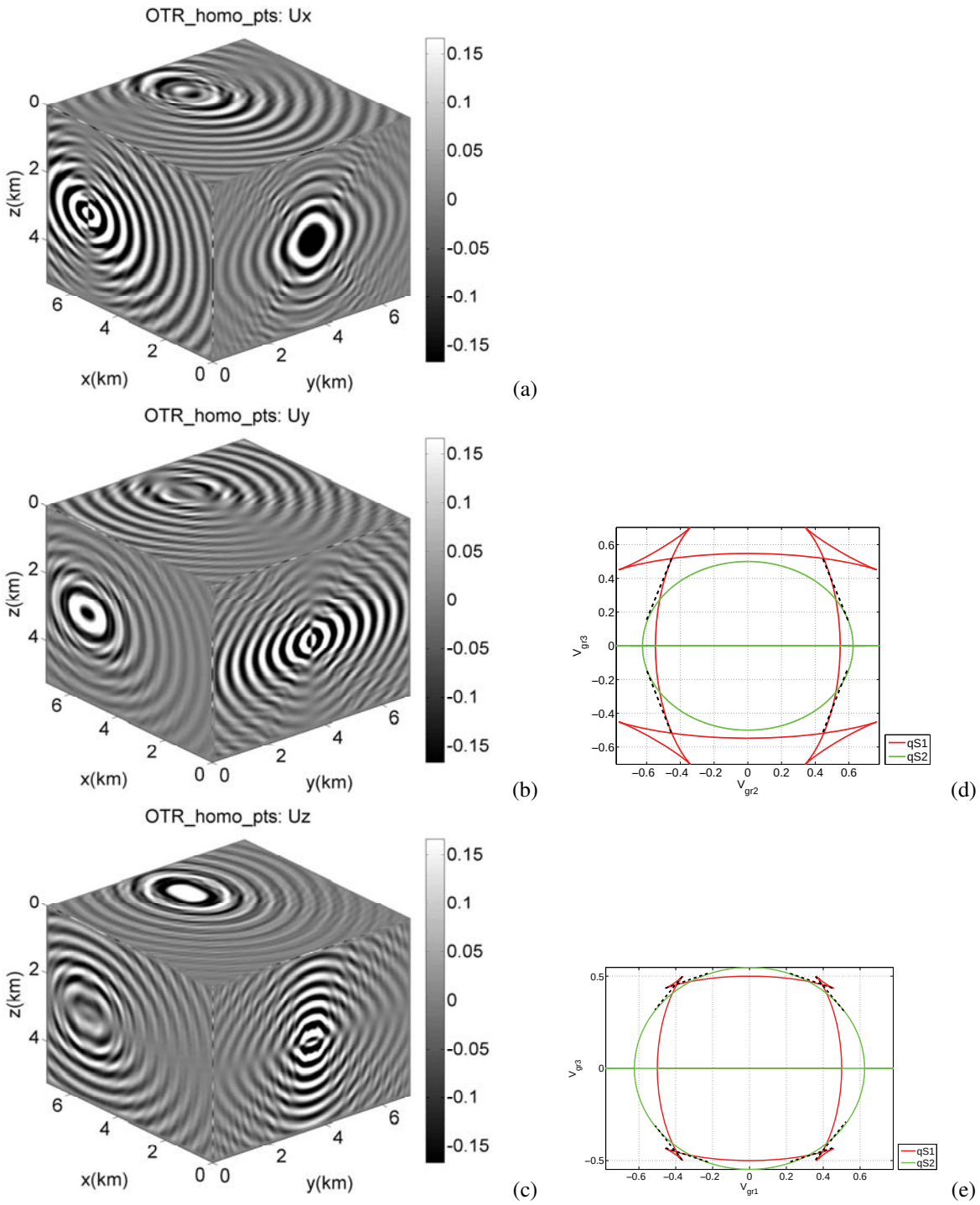


FIG. 11. *Multi-component time harmonic wavefield generated by an explosive point source in the homogeneous orthorhombic model with parameters depicted in Figure 8 and additional parameters:* $\epsilon^{(1)} = 0.2$, $\epsilon^{(2)} = 0.45$, $\delta^{(1)} = -0.1$, $\delta^{(2)} = 0.2$, $\delta^{(3)} = -0.15$, $\gamma^{(1)} = 0.28$, $\gamma^{(2)} = 0.15$. *The explosive point source is located at* $(5.25, 3.5, 2.625)$*km. (a):* $u_1$ *displayed on the planes of* $x_1 = 6.125$*km,* $x_2 = 3.5$*km and* $x_3 = 3.5$*km; (b):* $u_2$ *displayed on the planes of* $x_1 = 5.25$*km,* $x_2 = 4.375$*km and* $x_3 = 3.5$*km; (c):* $u_3$ *displayed on the planes of* $x_1 = 5.25$*km,* $x_2 = 3.5$*km and* $x_3 = 3.5$*km; (d): The wave front in the symmetry plane* $x_2 = 3.5$*km; (e): The wave front in the symmetry plane* $x_1 = 5.25$*km.*

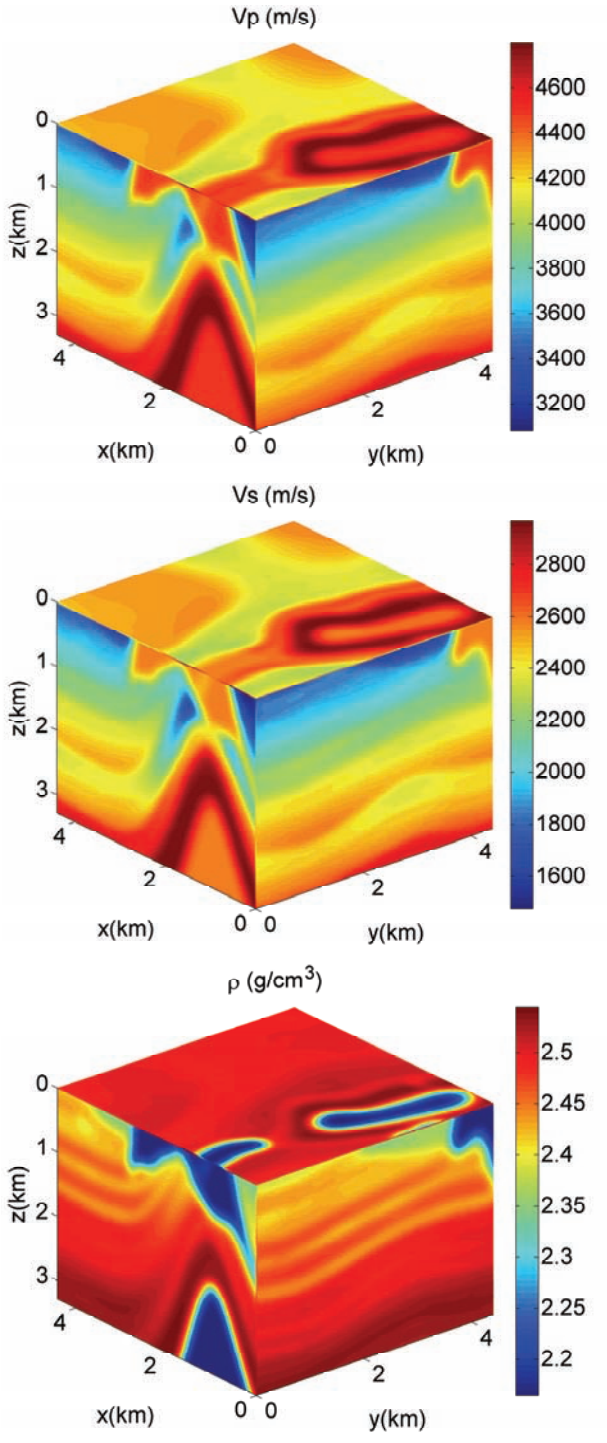


FIG. 12. *The inhomogeneous elastic VTI model discretized on a* $201 \times 201 \times 151$ *mesh with stepsizes* $h_1 = h_2 = h_3 = 0.022$*km. All models are displayed on the planes of* $x_1 = 3.3$*km,* $x_2 = 2.2$*km and* $x_3 = 1.65$*km. (a): "vertical" P-wave velocity* $V_p$*; (b): "vertical" S-wave velocity* $V_s$*; (c): density* $\rho$*.*

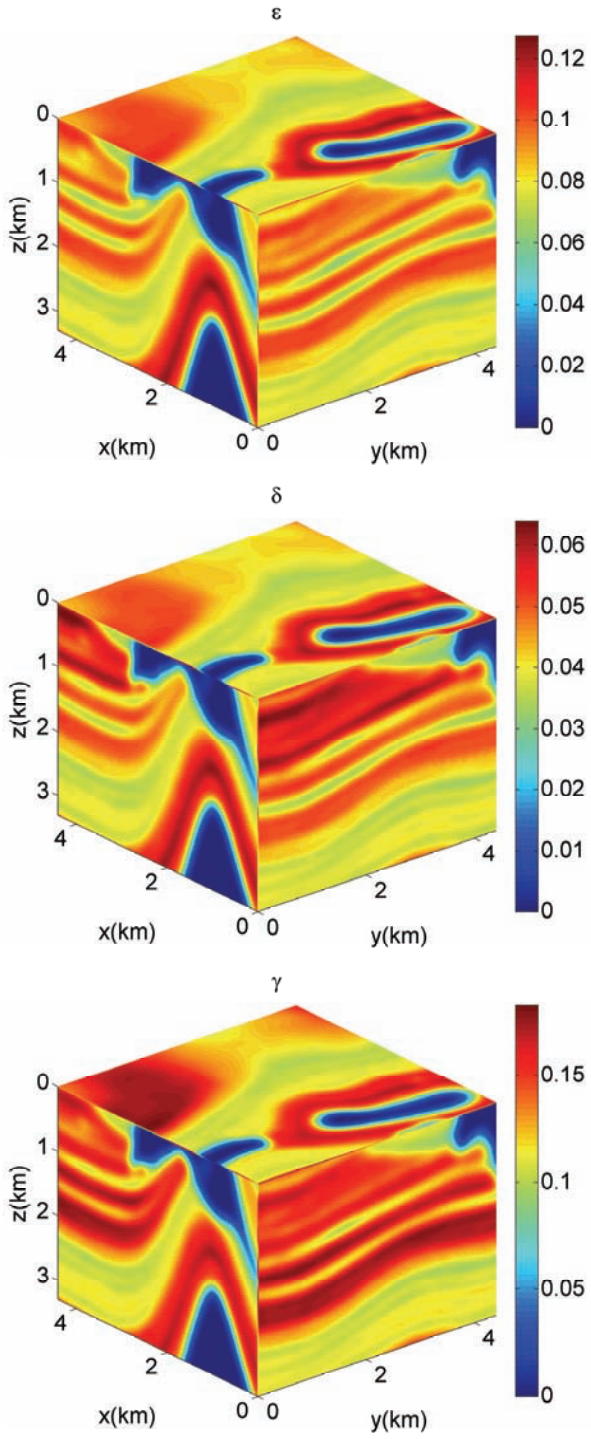


FIG. 13. *The inhomogeneous elastic VTI model discretized on a* $201 \times 201 \times 151$ *mesh with stepsizes* $h_1 = h_2 = h_3 = 0.022$*km. All models are displayed on the planes of* $x_1 = 3.3$*km,* $x_2 = 2.2$*km and* $x_3 = 1.65$*km. (a): Thomsen's parameter* $\epsilon$*; (b): Thomsen's parameter* $\delta$*; (c): Thomsen's parameter* $\gamma$*.*

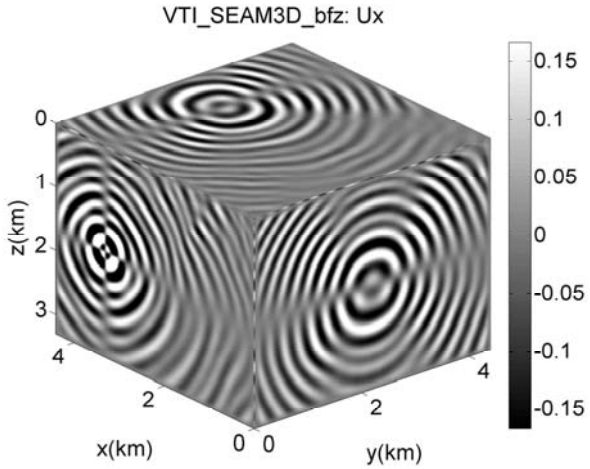


(a)

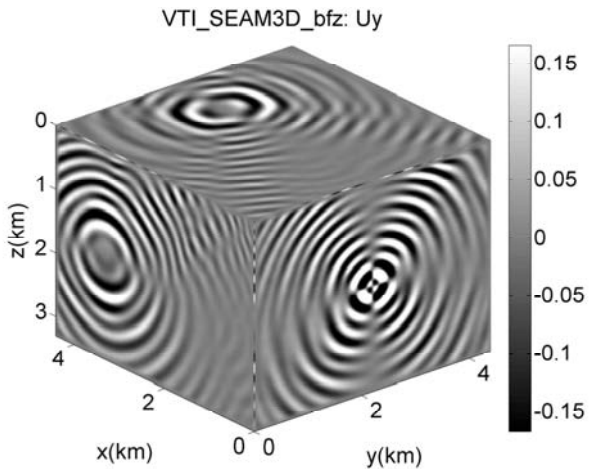


(b)

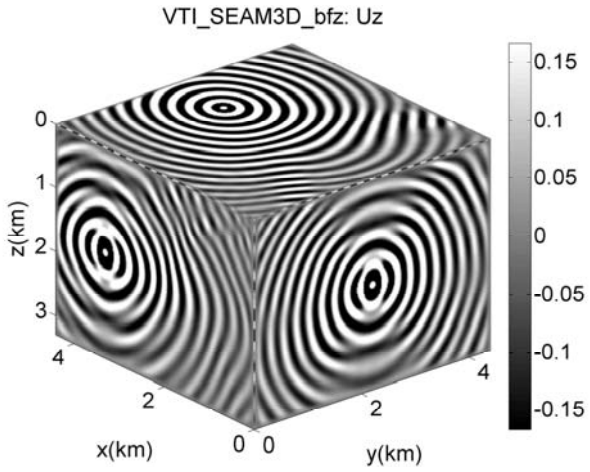


(c)

FIG. 14. *Multi-component time harmonic wavefield generated by a vertical point body force in the inhomogeneous VTI model depicted in Figures 12 and 13. The body force is located at* $(3.3, 2.2, 1.65)$*km. (a):* $u_1$ *displayed on the planes of* $x_1 = 3.85$*km,* $x_2 = 2.2$*km and* $x_3 = 2.2$*km; (b):* $u_2$ *displayed on the planes of* $x_1 = 3.3$*km,* $x_2 = 2.75$*km and* $x_3 = 2.2$*km; (c):* $u_3$ *displayed on the planes of* $x_1 = 3.3$*km,* $x_2 = 2.2$*km and* $x_3 = 1.65$*km.*

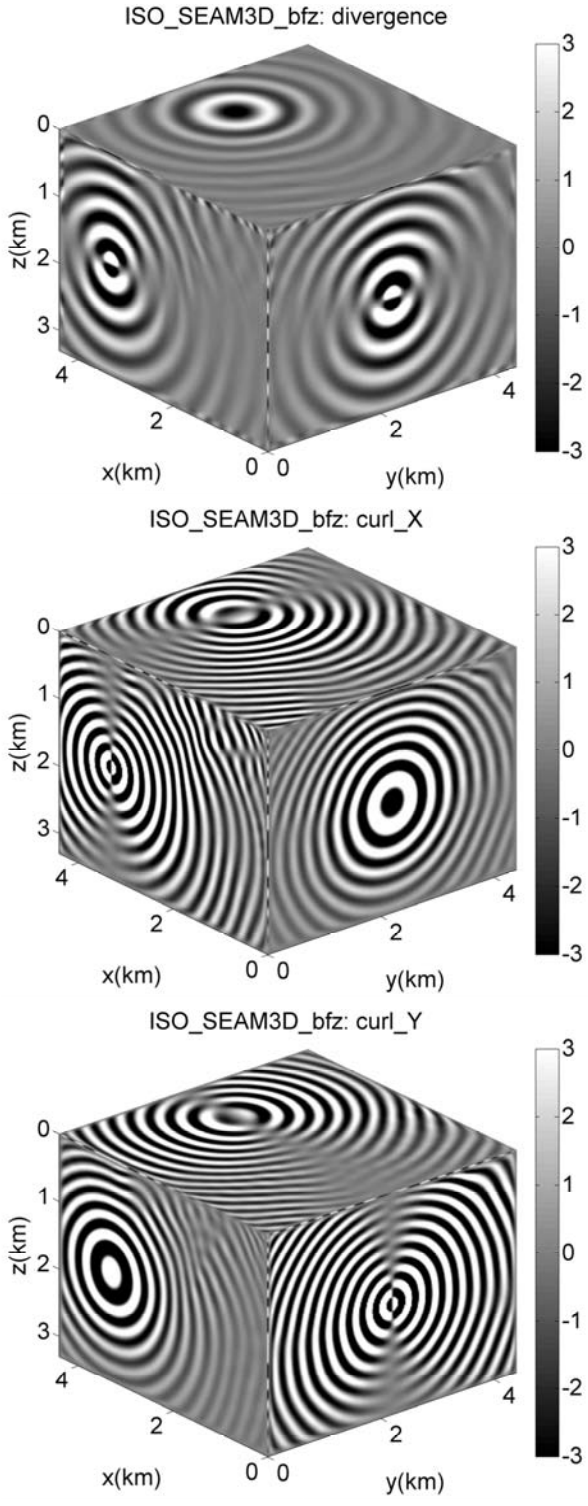


FIG. 15. *The divergence* $\nabla \cdot \mathbf{u}$ *and the curl* $\nabla \times \mathbf{u}$ *of the time-harmonic wavefield generated by a vertical point body force in the inhomogeneous elastic isotropic model depicted in Figure 12. The point body force is located at* $(3.3, 2.2, 1.65)$*km. (a):* $\nabla \cdot \mathbf{u}$ *displayed on the planes of* $x_1 = 3.3$*km,* $x_2 = 2.2$*km and* $x_3 = 2.2$*km; (b):* $(\nabla \times \mathbf{u})_1$ *displayed on the planes of* $x_1 = 3.85$*km,* $x_2 = 2.2$*km and* $x_3 = 1.65$*km; (c):* $(\nabla \times \mathbf{u})_2$ *displayed on the planes of* $x_1 = 3.3$*km,* $x_2 = 2.75$*km and* $x_3 = 1.65$*km.*

**Appendix A. The evaluation of $A_{11}$ in orthorhombic media.**

In this section, we present the evaluation of one entry $\widehat{A}_{11}(\mathbf{x},\omega)$ out of $\widehat{\mathbf{A}}(\mathbf{x},\omega)$ in equation (2.6), for orthorhombic media. For the sake of brevity, we denote the $u_1$ component as $v$, and normalize $A_{11}$ by the multiplication of $h^2$ where $h$ is the mesh stepsize. We recall that

$$A_{11}(\mathbf{x},\partial_{\mathbf{x}},\omega)=-\frac{\partial}{\partial x_1}\left(C_{11}\frac{\partial}{\partial x_1}\right)-\frac{\partial}{\partial x_2}\left(C_{66}\frac{\partial}{\partial x_2}\right)-\frac{\partial}{\partial x_3}\left(C_{55}\frac{\partial}{\partial x_3}\right).$$

Similar to equation (2.6), we have

$$A_{11}=w_{s1}A_{11}^{(c)}+\frac{w_{s2}}{3}\left(A_{11}^{(x)}+A_{11}^{(y)}+A_{11}^{(z)}\right)+\frac{w_{s3}}{4}\left(A_{11}^{(1)}+A_{11}^{(2)}+A_{11}^{(3)}+A_{11}^{(4)}\right);$$

here,

$$\begin{aligned}A_{11}^{(c)}=&\left[(C_{11})_{-\frac{1}{2}00}\left(v_{000}-v_{-100}\right)+(C_{11})_{\frac{1}{2}00}\left(v_{000}-v_{100}\right)\right]\\&+\left[(C_{66})_{0-\frac{1}{2}0}\left(v_{000}-v_{0-10}\right)+(C_{66})_{0\frac{1}{2}0}\left(v_{000}-v_{010}\right)\right]\\&+\left[(C_{55})_{00-\frac{1}{2}}\left(v_{000}-v_{00-1}\right)+(C_{55})_{00\frac{1}{2}}\left(v_{000}-v_{001}\right)\right];\end{aligned}$$

and

$$\begin{aligned}A_{11}^{(x)}=&\left[(C_{11})_{-\frac{1}{2}00}\left(v_{000}-v_{-100}\right)+(C_{11})_{\frac{1}{2}00}\left(v_{000}-v_{100}\right)\right]\\&+\frac{1}{4}\left[(C_{66})_{0-\frac{1}{2}\frac{1}{2}}\left(v_{000}-v_{0-11}\right)+(C_{66})_{0\frac{1}{2}-\frac{1}{2}}\left(v_{000}-v_{01-1}\right)\right]\\&+\frac{1}{4}\left[(C_{66})_{0-\frac{1}{2}-\frac{1}{2}}\left(v_{000}-v_{0-1-1}\right)+(C_{66})_{0\frac{1}{2}\frac{1}{2}}\left(v_{000}-v_{011}\right)\right]\\&+\frac{1}{4}\left[(C_{66})_{0\frac{1}{2}-\frac{1}{2}}\left(v_{010}-v_{00-1}\right)-(C_{66})_{0-\frac{1}{2}\frac{1}{2}}\left(v_{001}-v_{0-10}\right)\right]\\&+\frac{1}{4}\left[(C_{66})_{0\frac{1}{2}\frac{1}{2}}\left(v_{010}-v_{001}\right)-(C_{66})_{0-\frac{1}{2}-\frac{1}{2}}\left(v_{00-1}-v_{0-10}\right)\right]\\&+\frac{1}{4}\left[(C_{55})_{0-\frac{1}{2}\frac{1}{2}}\left(v_{000}-v_{0-11}\right)+(C_{55})_{0\frac{1}{2}-\frac{1}{2}}\left(v_{000}-v_{01-1}\right)\right]\\&+\frac{1}{4}\left[(C_{55})_{0-\frac{1}{2}-\frac{1}{2}}\left(v_{000}-v_{0-1-1}\right)+(C_{55})_{0\frac{1}{2}\frac{1}{2}}\left(v_{000}-v_{011}\right)\right]\\&-\frac{1}{4}\left[(C_{55})_{0\frac{1}{2}-\frac{1}{2}}\left(v_{010}-v_{00-1}\right)-(C_{55})_{0-\frac{1}{2}\frac{1}{2}}\left(v_{001}-v_{0-10}\right)\right]\\&-\frac{1}{4}\left[(C_{55})_{0\frac{1}{2}\frac{1}{2}}\left(v_{010}-v_{001}\right)-(C_{55})_{0-\frac{1}{2}-\frac{1}{2}}\left(v_{00-1}-v_{0-10}\right)\right];\end{aligned}$$

similar expressions are obtained for $A_{11}^{(y)}$ and $A_{11}^{(z)}$. Moreover,

$$
\begin{aligned}
A_{11}^{(1)} =& \frac{1}{4}\left[(C_{11})_{-\frac{1}{2}\frac{1}{2}\frac{1}{2}}\left(v_{000}-v_{-111}\right)+(C_{11})_{\frac{1}{2}-\frac{1}{2}-\frac{1}{2}}\left(v_{000}-v_{1-1-1}\right)\right] \\
&+\frac{1}{4}\left[(C_{11})_{\frac{1}{2}\frac{1}{2}-\frac{1}{2}}\left(v_{000}-v_{11-1}\right)+(C_{11})_{-\frac{1}{2}-\frac{1}{2}\frac{1}{2}}\left(v_{000}-v_{-1-11}\right)\right] \\
&-\frac{1}{4}\left[(C_{11})_{-\frac{1}{2}\frac{1}{2}\frac{1}{2}}\left(v_{010}-v_{-101}\right)-(C_{11})_{\frac{1}{2}-\frac{1}{2}-\frac{1}{2}}\left(v_{10-1}-v_{0-10}\right)\right] \\
&-\frac{1}{4}\left[(C_{11})_{\frac{1}{2}\frac{1}{2}-\frac{1}{2}}\left(v_{010}-v_{10-1}\right)-(C_{11})_{-\frac{1}{2}-\frac{1}{2}\frac{1}{2}}\left(v_{-101}-v_{0-10}\right)\right] \\
&+\frac{1}{4}\left[(C_{66})_{\frac{1}{2}\frac{1}{2}\frac{1}{2}}\left(v_{000}-v_{111}\right)+(C_{66})_{-\frac{1}{2}-\frac{1}{2}-\frac{1}{2}}\left(v_{000}-v_{-1-1-1}\right)\right] \\
&+\frac{1}{4}\left[(C_{66})_{\frac{1}{2}\frac{1}{2}-\frac{1}{2}}\left(v_{000}-v_{11-1}\right)+(C_{66})_{-\frac{1}{2}-\frac{1}{2}\frac{1}{2}}\left(v_{000}-v_{-1-11}\right)\right] \\
&+\frac{1}{4}\left[(C_{66})_{\frac{1}{2}\frac{1}{2}-\frac{1}{2}}\left(v_{110}-v_{00-1}\right)-(C_{66})_{-\frac{1}{2}-\frac{1}{2}\frac{1}{2}}\left(v_{001}-v_{-1-10}\right)\right] \\
&+\frac{1}{4}\left[(C_{66})_{\frac{1}{2}\frac{1}{2}\frac{1}{2}}\left(v_{110}-v_{001}\right)-(C_{66})_{-\frac{1}{2}-\frac{1}{2}-\frac{1}{2}}\left(v_{00-1}-v_{-1-10}\right)\right] \\
&+\frac{1}{4}\left[(C_{55})_{\frac{1}{2}\frac{1}{2}\frac{1}{2}}\left(v_{000}-v_{111}\right)+(C_{55})_{-\frac{1}{2}-\frac{1}{2}-\frac{1}{2}}\left(v_{000}-v_{-1-1-1}\right)\right] \\
&+\frac{1}{4}\left[(C_{55})_{-\frac{1}{2}\frac{1}{2}\frac{1}{2}}\left(v_{000}-v_{-111}\right)+(C_{55})_{\frac{1}{2}-\frac{1}{2}-\frac{1}{2}}\left(v_{000}-v_{1-1-1}\right)\right] \\
&+\frac{1}{4}\left[(C_{55})_{\frac{1}{2}\frac{1}{2}\frac{1}{2}}\left(v_{011}-v_{100}\right)-(C_{55})_{-\frac{1}{2}-\frac{1}{2}-\frac{1}{2}}\left(v_{-100}-v_{0-1-1}\right)\right] \\
&+\frac{1}{4}\left[(C_{55})_{-\frac{1}{2}\frac{1}{2}\frac{1}{2}}\left(v_{011}-v_{-100}\right)-(C_{55})_{\frac{1}{2}-\frac{1}{2}-\frac{1}{2}}\left(v_{100}-v_{0-1-1}\right)\right],
\end{aligned}
$$

and similar expressions are obtained for $A_{11}^{(2)}$, $A_{11}^{(3)}$ and $A_{11}^{(4)}$. Here the subscript $\frac{1}{2}$ denotes the interpolation of the stiffness tensor, following the notation in [14].

Conversely, we find the weighting for each grid point,

$$
\begin{aligned}
v_{000}:\ &\left(w_{s1}+\frac{w_{s2}}{3}\right)\Big[(C_{11})_{-\frac{1}{2}00}+(C_{11})_{\frac{1}{2}00}+(C_{66})_{0-\frac{1}{2}0}+(C_{66})_{0\frac{1}{2}0}+(C_{55})_{00-\frac{1}{2}}+(C_{55})_{00\frac{1}{2}}\Big] \\
&+\frac{w_{s2}}{12}\Big[(C_{66})_{0-\frac{1}{2}-\frac{1}{2}}+(C_{66})_{0\frac{1}{2}-\frac{1}{2}}+(C_{66})_{0-\frac{1}{2}\frac{1}{2}}+(C_{66})_{0\frac{1}{2}\frac{1}{2}} \\
&+(C_{55})_{0-\frac{1}{2}-\frac{1}{2}}+(C_{55})_{0\frac{1}{2}-\frac{1}{2}}+(C_{55})_{0-\frac{1}{2}\frac{1}{2}}+(C_{55})_{0\frac{1}{2}\frac{1}{2}} \\
&+(C_{11})_{-\frac{1}{2}0-\frac{1}{2}}+(C_{11})_{\frac{1}{2}0-\frac{1}{2}}+(C_{11})_{-\frac{1}{2}0\frac{1}{2}}+(C_{11})_{\frac{1}{2}0\frac{1}{2}} \\
&+(C_{55})_{-\frac{1}{2}0-\frac{1}{2}}+(C_{55})_{\frac{1}{2}0-\frac{1}{2}}+(C_{55})_{-\frac{1}{2}0\frac{1}{2}}+(C_{55})_{\frac{1}{2}0\frac{1}{2}} \\
&+(C_{11})_{-\frac{1}{2}-\frac{1}{2}0}+(C_{11})_{\frac{1}{2}-\frac{1}{2}0}+(C_{11})_{-\frac{1}{2}\frac{1}{2}0}+(C_{11})_{\frac{1}{2}\frac{1}{2}0} \\
&+(C_{66})_{-\frac{1}{2}-\frac{1}{2}0}+(C_{66})_{\frac{1}{2}-\frac{1}{2}0}+(C_{66})_{-\frac{1}{2}\frac{1}{2}0}+(C_{66})_{\frac{1}{2}\frac{1}{2}0}\Big] \\
&+\frac{w_{s3}}{16}\Big[(C_{11})_{-\frac{1}{2}-\frac{1}{2}-\frac{1}{2}}+(C_{11})_{\frac{1}{2}-\frac{1}{2}-\frac{1}{2}}+(C_{11})_{-\frac{1}{2}\frac{1}{2}-\frac{1}{2}}+(C_{11})_{\frac{1}{2}\frac{1}{2}-\frac{1}{2}} \\
&+(C_{11})_{-\frac{1}{2}-\frac{1}{2}\frac{1}{2}}+(C_{11})_{\frac{1}{2}-\frac{1}{2}\frac{1}{2}}+(C_{11})_{-\frac{1}{2}\frac{1}{2}\frac{1}{2}}+(C_{11})_{\frac{1}{2}\frac{1}{2}\frac{1}{2}} \\
&+(C_{66})_{-\frac{1}{2}-\frac{1}{2}-\frac{1}{2}}+(C_{66})_{\frac{1}{2}-\frac{1}{2}-\frac{1}{2}}+(C_{66})_{-\frac{1}{2}\frac{1}{2}-\frac{1}{2}}+(C_{66})_{\frac{1}{2}\frac{1}{2}-\frac{1}{2}} \\
&+(C_{66})_{-\frac{1}{2}-\frac{1}{2}\frac{1}{2}}+(C_{66})_{\frac{1}{2}-\frac{1}{2}\frac{1}{2}}+(C_{66})_{-\frac{1}{2}\frac{1}{2}\frac{1}{2}}+(C_{66})_{\frac{1}{2}\frac{1}{2}\frac{1}{2}} \\
&+(C_{55})_{-\frac{1}{2}-\frac{1}{2}-\frac{1}{2}}+(C_{55})_{\frac{1}{2}-\frac{1}{2}-\frac{1}{2}}+(C_{55})_{-\frac{1}{2}\frac{1}{2}-\frac{1}{2}}+(C_{55})_{\frac{1}{2}\frac{1}{2}-\frac{1}{2}} \\
&+(C_{55})_{-\frac{1}{2}-\frac{1}{2}\frac{1}{2}}+(C_{55})_{\frac{1}{2}-\frac{1}{2}\frac{1}{2}}+(C_{55})_{-\frac{1}{2}\frac{1}{2}\frac{1}{2}}+(C_{55})_{\frac{1}{2}\frac{1}{2}\frac{1}{2}}\Big],
\end{aligned}
$$

and

$$
\begin{aligned}
v_{100}:\ &-\left(w_{s1}+\frac{w_{s2}}{3}\right)(C_{11})_{\frac{1}{2}00}\\
&-\frac{w_{s2}}{12}\left[2\,(C_{11})_{\frac{1}{2}-\frac{1}{2}0}+2\,(C_{11})_{\frac{1}{2}\frac{1}{2}0}-(C_{66})_{\frac{1}{2}-\frac{1}{2}0}-(C_{66})_{\frac{1}{2}\frac{1}{2}0}-(C_{55})_{\frac{1}{2}-\frac{1}{2}0}-(C_{55})_{\frac{1}{2}\frac{1}{2}0}\right]\\
&-\frac{w_{s3}}{16}\left[(C_{55})_{\frac{1}{2}-\frac{1}{2}-\frac{1}{2}}+(C_{55})_{\frac{1}{2}\frac{1}{2}-\frac{1}{2}}+(C_{55})_{\frac{1}{2}-\frac{1}{2}\frac{1}{2}}+(C_{55})_{\frac{1}{2}\frac{1}{2}\frac{1}{2}}\right.\\
&\left.+\,(C_{66})_{\frac{1}{2}-\frac{1}{2}-\frac{1}{2}}+(C_{66})_{\frac{1}{2}\frac{1}{2}-\frac{1}{2}}+(C_{66})_{\frac{1}{2}-\frac{1}{2}\frac{1}{2}}+(C_{66})_{\frac{1}{2}\frac{1}{2}\frac{1}{2}}\right],
\end{aligned}
$$

while similar results are obtained for $v_{-100}$, $v_{0-10}$, $v_{010}$, $v_{00-1}$ and $v_{001}$. Moreover,

$$
\begin{aligned}
v_{110}:\ &-\frac{w_{s2}}{12}\left[(C_{11})_{\frac{1}{2}\frac{1}{2}0}+(C_{66})_{\frac{1}{2}\frac{1}{2}0}\right]\\
&-\frac{w_{s3}}{16}\left[(C_{11})_{\frac{1}{2}\frac{1}{2}-\frac{1}{2}}+(C_{11})_{\frac{1}{2}\frac{1}{2}\frac{1}{2}}+(C_{66})_{\frac{1}{2}\frac{1}{2}-\frac{1}{2}}+(C_{66})_{\frac{1}{2}\frac{1}{2}\frac{1}{2}}\right],
\end{aligned}
$$

while similar results are obtained for $v_{-1-10}$, $v_{1-10}$, $v_{-110}$, $v_{-10-1}$, $v_{10-1}$, $v_{-101}$, $v_{101}$, $v_{0-1-1}$, $v_{01-1}$, $v_{0-11}$ and $v_{011}$. Finally,

$$
v_{111}:\ -\frac{w_{s3}}{8}\left[(C_{11})_{\frac{1}{2}\frac{1}{2}\frac{1}{2}}+(C_{66})_{\frac{1}{2}\frac{1}{2}\frac{1}{2}}+(C_{55})_{\frac{1}{2}\frac{1}{2}\frac{1}{2}}\right],
$$

while similar results are obtained for $v_{-1-1-1}$, $v_{1-1-1}$, $v_{-11-1}$, $v_{11-1}$, $v_{-1-11}$, $v_{1-11}$ and $v_{-111}$.

## REFERENCES


[1] E. AGULLO, A. GUERMOUCHE, AND J.Y. L'EXCELLENT, *A parallel out-of-core multifrontal method: Storage of factors on disk and analysis of models for an out-of-core active memory*, Parallel Computing, 34 (2008), pp. 296–317.

[2] T. AIRAKSINEN, A. PENNANEN, AND J. TOIVANNEN, *A damping preconditioner for time-harmonic wave equations in fluid and elastic material*, J. Comput. Physics, 228 (2009), pp. 1466–1479.

[3] B. ALPERT, G. BEYLKIN, R. COIFMAN, AND V. ROKHLIN, *Wavelet-like bases for the fast solution of second-kind integral equations*, SIAM J. Sci. Comput., 14 (1993), pp. 159–184.

[4] R. BANSAL AND M.K. SEN, *Finite-difference modeling of S-wave splitting in anisotropic media*, Geophysical Prospecting, 56 (2008), pp. 293–312.

[5] V. BRYTIK, M.V. DE HOOP, AND R.D. VAN DER HILST, *Elastic-wave inverse scattering with active and passive source reflection data*, submitted, (2011).

[6] I. ŠTEKL AND G.R. PRATT, *Accurate viscoelastic modeling by frequency-domain finite differences using rotated operators*, Geophysics, 63 (1998), pp. 1779–1794.

[7] A. EL KACIMI AND O. LAGHROUCHE, *Wavelet based $ILU$ preconditioners for the numerical solution by PUFEM of high frequency elastic wave scattering*, J. Comput. Physics, 230 (2011), pp. 3119–3134.

[8] A. FICHTNER, H. IGEL, H.P. BUNGE, AND B.L.N. KENNETT, *Simulation and inversion of seismic wave propagation on continental scales based on a spectral-element method*, Journal of Numerical Analysis, Industrial and Applied Mathematics, 4 (2009), pp. 11–22.

[9] P.M. GAUZELLINO, J.E. SANTOS, AND D. SHEEN, *Frequency domain wave propagation modeling in exploration seismology*, J. of computational acoustics, 9 (2001), pp. 941–955.

[10] J.A. GEORGE, *Nested dissection of a regular finite element mesh*, SIAM J. Numer. Anal., 10 (1973), pp. 345–363.

[11] O. HOLBERG, *Computational aspects of the choice of operator and sampling interval for numerical differentiation in large-scale simulation of wave phenomena*, Geophysical Prospecting, 35 (1987), pp. 629–655.

[12] J. JR. DOUGLAS, D. SHEEN, AND J.E. SANTOS, *Approximation of scalar waves in the space-frequency domain*, Mathematical Models and Methods in Applied Sciences, 4 (1994), pp. 509–531.

[13] J.W.H. LIU, *The multifrontal method for sparse matrix solution: Theory and practice*, SIAM Review, 34 (1992), pp. 82–109.

[14] S. OPERTO, J. VIRIEUX, P. AMESTOY, J.Y. L'EXCELLENT, L. GIRAUD, AND H.B. HADJ ALI, *3D finite-difference frequency-domain modeling of visco-acoustic wave propagation using a massively parallel direct solver: A feasibility study*, Geophysics, 72 (2007), pp. SM195–SM211.

[15] R.G. PRATT, *Frequency-domain elastic wave modeling by finite differences: A tool for crosshole seismic imaging*, Geophysics, 55 (1990), pp. 626–632.

[16] C.C. STOLK AND M.V. DE HOOP, *Microlocal analysis of seismic inverse scattering in anisotropic elastic media*, Communications on Pure and Applied Mathematics, 55 (2002), pp. 261–301.

[17] L. THOMSEN, *Weak elastic anisotropy*, Geophysics, 51 (1986), pp. 1954–1966.

[18] J. TROMP, D. KOMATITSCH, AND Q. LIU, *Spectral-element and adjoint methods in seismology*, Commun. in Comput. Phys., 3 (2008), pp. 1–32.

[19] I. TSVANKIN, *Anisotropic parameters and P-wave velocity for orthorhombic media*, Geophysics, 62 (1997), pp. 1292–1309.
[20] M.J.N. VAN STRALEN, M.V. DE HOOP, AND H. BLOK, *Generalized bremmer series with rational approximation for the scattering of waves in inhomogeneous media*, J. Acoust. Soc. Am., 104 (1998), pp. 1943–1963.
[21] S. WANG, M.V. DE HOOP, AND J. XIA, *Seismic inverse scattering via Helmholtz operator factorization and optimization*, Journal of Computational Physics, 229 (2010), pp. 8445–8462.
[22] S. WANG, M.V. DE HOOP, AND J. XIA, *On 3D modeling of seismic wave propagation via a structured parallel multifrontal direct Helmholtz solver*, Geophysical Prospecting, 59 (2011), pp. 857–873.
[23] S. WANG, X.S. LI, J. XIA, Y.C. SITU, AND M.V. DE HOOP, *Efficient scalable algorithms for hierarchically semiseparable matrices*, submitted to SIAM J. Sci. Comput., (2011).
[24] S. WANG, J. XIA, M.V. DE HOOP, AND X.S. LI, *Massively parallel structured direct solver for equations describing time-harmonic qp-polarized waves in TTI media*, to appear, Geophysics, (2012).
[25] J. XIA, *Efficient structured multifrontal factorization for general large sparse matrices*, submitted to SIAM J. Sci. Comput., http://www.math.purdue.edu/∼xiaj/work/mfhss.pdf, (2012).
[26] ———, *On the complexity of some hierarchical structured matrices*, to appear, SIAM J. Matrix Anal. Appl., (2012).
[27] J. XIA, S. CHANDRASEKARAN, M. GU, AND X.S. LI, *Superfast multifrontal method for large structured linear systems of equations*, SIAM J. Matrix Anal. Appl., 31 (2009), pp. 1382–1411.
[28] ———, *Fast algorithms for hierarchically semiseparable matrices*, Numer. Linear Algebra Appl., 17 (2010), pp. 953–976.